LBL-26859
Preprint

Lawrence Berkeley Laboratory
UNIVERSITY OF CALIFORNIA

Submitted to Nuclear Physics

# Sources of Complex Fragment Emission in Lanthanum-Induced Reactions at E/A = 14.7 and 18.0 MeV

R.J. Charity, K.X. Jing, D.R. Bowman, M.A. McMahan,
G.J. Wozniak, L.G. Moretto, N. Colonna, G. Guarino,
A. Pantaleo, L. Fiore, A. Gobbi, and K.D. Hildenbrand

July 1989

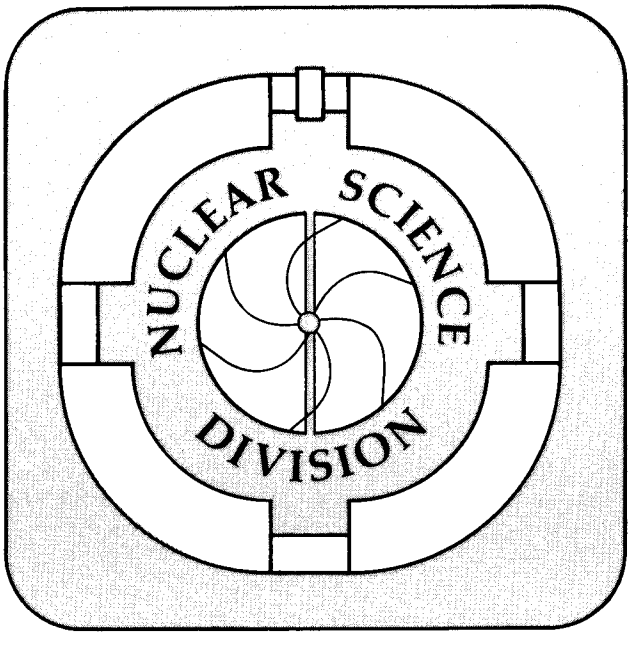


| LOAN COPY |
|Circulates |
|for 2 weeks|
Bldg. 50 Library.
Copy 2
LBL-26859

Prepared for the U.S. Department of Energy under Contract Number DE-AC03-76SF00098.

## DISCLAIMER

This document was prepared as an account of work sponsored by the United States Government. While this document is believed to contain correct information, neither the United States Government nor any agency thereof, nor the Regents of the University of California, nor any of their employees, makes any warranty, express or implied, or assumes any legal responsibility for the accuracy, completeness, or usefulness of any information, apparatus, product, or process disclosed, or represents that its use would not infringe privately owned rights. Reference herein to any specific commercial product, process, or service by its trade name, trademark, manufacturer, or otherwise, does not necessarily constitute or imply its endorsement, recommendation, or favoring by the United States Government or any agency thereof, or the Regents of the University of California. The views and opinions of authors expressed herein do not necessarily state or reflect those of the United States Government or any agency thereof or the Regents of the University of California.

LBL-26859

# SOURCES OF COMPLEX FRAGMENT EMISSION IN LANTHANUM-INDUCED REACTIONS AT E/A = 14.7 AND 18.0 MeV.*

R.J. CHARITY[1], K.X. JING[2], D.R. BOWMAN, M.A. McMAHAN, G.J. WOZNIAK, and L.G. MORETTO
*Nuclear Science Division, Lawrence Berkeley Laboratory, 1 Cyclotron Rd., Berkeley, California, 94720, USA.*

N. COLONNA[3], G. GUARINO, A. PANTALEO, and L. FIORE
*Istituto Nazionale di Fisica Nucleare INFN, Sezione di Bari, Italy.*

A. GOBBI and K.D. HILDENBRAND
*Gesellschaft für Schwerionenforschung, 6100 Darmstadt, West Germany.*

**Abstract:** Complex fragments with $4 \leq Z \lesssim 50$ have been detected in the reactions of $^{139}La + ^{12}C$ and $^{27}Al$ at E/A = 14.7 & 18.0 MeV. From the measured angular distributions, the cross sections for the isotropic, target-like and projectile-like components were extracted. The roles of deep-inelastic, fast-fission, and incomplete fusion processes, and the statistical, compound nucleus emission of complex fragments are discussed.

NUCLEAR REACTIONS $^{12}C$,$^{27}Al$($^{139}La$,X), E=14.7, 18.0 MeV/nucleon; measured fragment $\sigma$(fragment E, $\theta$), (fragment)(fragment)-coin. Statistical model calculations.

[1]Present Address: Gesellschaft für Schwerionenforschung, Darmstadt, West Germany.
[2]Permanent Address: Institute of Atomic Energy, Beijing, China.
[3]Present Address: Lawrence Berkeley Laboratory, Nuclear Science Division, Berkeley, CA, USA.

# 1 Introduction

The production of complex fragment ($Z \geq 3$) in heavy-ion induced reactions is presently a subject of great interest. Complex fragment emission has been observed both at low and at intermediate bombarding energies. At the lower energies ($E/A \leq 50$ MeV), two components are easily identified. The first is the "isotropic", "equilibrium", or "compound nucleus" source[1-11]. It it associated with binary processes which cover the entire range of mass-asymmetry. The fragments are emitted with Coulomb-like velocities and $1/\sin\theta$ angular distributions in the center-of-mass frame. This source has been shown to originate from the statistical decay of a compound nucleus (CN) as suggested by Moretto[12]. The compound nucleus is formed in either fusion, or, at the larger bombarding energies, an incomplete fusion process. For some reactions it is also suggested that fast-fission processes may contribute[6].

The second component, which has been termed the "deep-inelastic", "non-equilibrium", or "intermediate velocity" source[1-4,6,8-10,13-15] is characterized by mass yields for the lighter fragments which follow an approximate power-law dependence. The angular distributions of these fragments are forward peaked in normal kinematic reactions. (In reverse kinematic reactions the angular distributions are of course backward peaked). The origin of this component has been the subject of some speculation. Models originally proposed to explain the production of these fragments include phase transitions, coalescence, local equilibrium and cold cracking. However, this component is also predominantly binary. It is associated with the larger mass-asymmetries and seems to evolve continuously from lower energies, where it is unequivocally identified with the traditional quasi-elastic and deep-inelastic processes.

At higher bombarding energies, the processes governing the production of complex fragments are even less clear. One observes an increasing yield of 3-body and higher order events as the bombarding energy increases. The question of whether these events are associated with true multifragmentation exit-channels, or are produced by several sequential binary decays is the subject of much debate

at present. The latter mechanism is a logical evolution of the lower energy, binary processes. As the excitation energy of the fragments produced in an initial binary event (whether associated with either the isotropic or the deep-inelastic component) increases, it becomes possible for one, or both, of the fragments to undergo further sequential binary decays. Thus, a good understanding of the lower energy processes may allow one to characterize these higher order events.

The probability P of emitting a complex fragment in the statistical model is determined by the conditional barrier B for each binary division and by the nuclear temperature T at the barrier and follows the approximate relationship $P \propto \exp(-B/T)$[12]. The conditional barriers represent the height of the ridge-line in the potential energy surface defined as the locus of the mass-asymmetric saddle-points. The dependence of the conditional barriers on the asymmetry of the binary division determines the charge or mass distribution of the emitted fragments. For a heavy CN above the Businaro-Gallone point[16], the ridge-line has a minimum height for symmetric division giving rise to the well known fission peak in the mass distribution. The ridge-line also reaches a minimum at the largest mass-asymmetries producing the other well known CN decay mode, light particle evaporation. For lighter CN, the fission-peak vanishes and the mass distributions are "U" shaped with a minimum corresponding to symmetric division.

Conditional barriers have been calculated with macroscopic models. A large number of studies[17-22] have compared experimental fission cross sections to statistical model predictions, utilizing Rotating-Liquid-Drop-Model (RLDM)[23] symmetric barriers. These studies suggest that the RLDM barriers need to be reduced in order to reproduce the experimental data. This conclusion is in agreement with more refined calculations of fission barriers made with the Rotating-Finite-Range-Model (RFRM)[24]. This model includes the effect of the finite range of the nuclear force and the diffuseness of the nuclear surface which are neglected in the RLDM. The predictions of these two models show the largest differences for light systems. Recent studies[6,25,26] in the $A \approx 100$ region find that

the RFRM barriers can adequately reproduce complex fragment cross sections. In order to test this model more rigorously, charge distributions of statistically emitted complex fragments need to be measured for lighter and heavier compound nuclei. Measurements of this kind may also allow for improved determination of some RFRM parameters.

In this work, we report on investigations of complex fragment emission in the reactions $^{139}$La + $^{12}$C & $^{27}$Al at bombarding energies of E/A = 14.7 and 18.0 MeV. These investigations constitute an extension to heavier mass systems of previous studies[5-9] of complex fragment emission in reverse kinematic experiments (E/A$\leq$50 MeV). The use of reverse kinematics with improved detectors has allowed us to obtain almost complete angular coverage of the fragment emission. This has proven most useful for separating the different fragment sources. The measured charge distributions for the isotropic component are compared to statistical model calculations to determine if this component is associated with CN decay and gauge the applicability of the RFRM in this mass region.

The experimental details of this work are discussed in Section 2. The results of the measurements and the separation of the complex fragment sources are presented in Section 3. In Section 4, the results are discussed and the experimental charge distributions are compared to statistical model calculations. Finally the conclusions are presented in Section 5.

# 2 Experimental Method

The experiment was performed at the Unilac at Gesellschaft für Schwerionenforschung. Beams of $^{139}$La projectiles with energies of E/A = 14.7 & 18.0 MeV impinged on targets of $^{12}$C (0.4 mg/cm$^2$) & $^{27}$Al (1.4 mg/cm$^2$).

Complex fragments were identified in two detectors each containing four $\Delta$E-E telescopes. Each telescope consisted of a gas ionization counter followed by a 5 mm thick, Li-drifted Si counter with surface dimensions of 5x5 cm$^2$. The ionization counters were filled with 60 torr of $CF_4$ gas and the energy lost ($\Delta$E) by the fragments in traversing 7 cm of the gas was measured. The residual energy

(E) of the fragments was measured with the Si counter. Each telescope subtended 5° both in- and out-of-plane and was position sensitive in two directions. The out-of-plane position was obtained from the drift time of the electrons in the ionization counter and the in-plane position from the voltage division across a resistive Pd-layer evaporated on the front surface of the Si counter.

Within each multi-telescope detector, the telescopes were located in a plane, with a separation between the active edges of adjacent telescopes of 1.6°. Thus, a single detector covered an angular range of 24.8° in-plane. Measurements were performed with the detectors located on either side of the beam axis in a number of different angular configurations. Initially both detectors were positioned to cover angles from 4° to 28.8°. For the second configuration, one detector was then moved to cover angles from 29° to 53.8°. Measurements were also performed at two other similar configurations where both detectors were moved a further 3° out from the beam. This allowed fragments to be detected at angles which were initially located in the dead areas between adjacent telescopes. From these four configurations a continuous coverage of angles between 4° and 56.8° was obtained. For the lower bombarding energy, an extra configuration was used, which extended the angular coverage to 64.8°. Singles and coincidence events between any two telescopes were recorded for each experimental configuration.

Energy and position calibrations of the $\Delta$E and E counters were obtained with elastically scattered $^{139}$La projectiles from a 0.5 mg/cm$^2$ thick $^{197}$Au target, using the methods described in Ref. 5.

Absolute cross sections were determined from the beam charge collected in a Faraday cup. Inclusive and coincidence events were recorded on magnetic tape and analyzed off-line.

# 3 Results

## 3.1 Velocity Plots

The velocity of a complex fragment was estimated from its measured kinetic energy using the mass parameterization of Ref. 5, which is thought to be valid

for secondary fragments which have undergone extensive evaporation. From these derived velocities and from the measured scattering angles, contour plots of $\partial^2\sigma/\partial V_{\|}\partial V_{\perp}$ in the $V_{\|}$-$V_{\perp}$ plane were constructed for each element. Some representative examples of these contour plots are shown for the E/A=18.0 MeV reactions in Figs. 1 & 2. The dashed curves in these figures indicate the lower velocity threshold and the smallest angle for which fragments were detected (4°). For the larger Z-values, the contour plots show only a prominent Coulomb ring. These rings were also observed in the $^{63}$Cu, $^{93}$Nb + $^{9}$Be, $^{12}$C, & $^{27}$Al reactions in Refs. 5, 6 & 8 and are a signature of the isotropic component. The center of a ring defines the laboratory velocity of the source system (compound nucleus or composite system), and the radius defines the (Coulomb) velocity with which the fragments are emitted from such a source system. For the lighter fragments, the Coulomb rings are still visible at the forward center-of-mass angles. However, at the backward angles they are masked by the target-like deep-inelastic component.

## 3.2 Source Velocities

The isotropic component has a characteristic source velocity which was extracted from the Coulomb rings using the procedure described in Ref. 6. This procedure involves fitting the Coulomb rings to a circle. The velocity at the center of this circle is the experimental source velocity. Fig. 3 shows the extracted values of $V_{source}/V_{beam}$, as a function of Z-value, for each of the reactions studied. No results are shown for small Z-values where the presence of the target-like component obscured a large part of the Coulomb ring. Also for the reactions with E/A=14.7 MeV, no source velocities were obtained for fragments with Z<17, as significant parts of the Coulomb rings fell below the low-velocity threshold of the detectors.

The small error bar on each point in Fig. 3, indicates the error associated with the extraction process. Although these errors are not large, the possible systematic error associated with the energy calibration of the detectors and the mass parameterization is larger. The two large error bars in Fig. 3 give an

estimate of this error.

The experimental source velocities show very little dependence on the fragment Z-value as would be expected if all fragments are emitted from a similar source or intermediate system. The source velocities are also close in value to the center-of-mass velocity of the reactions as indicated by the dashed lines in Fig. 3, suggesting that the intermediate systems were produced in fusion-like reactions.

## 3.3 Emission-Velocities

Using the extracted source velocities, the emission-velocity ($V_e$) of all fragments in the reference frame of their respective source system was determined and their velocity spectrum constructed. For the smaller Z-values where no source velocity was determined, an extrapolated value was used. Figures 4 & 5 show the emission-velocity spectra for Z=5 fragments at various angles. At the most forward angles, the spectra are associated essentially only with the isotropic component. The maximum and the width of the velocity spectra increase in value at larger angles. This is due to the presence of the deep-inelastic component which is concentrated at these more backward angles. The spectra were integrated over a restricted angular range in order to avoid contamination from the deep-inelastic component. Examples of velocity spectra for the isotropic component are displayed in Figs. 6 & 7. The absolute normalization of the spectra have been corrected for the restricted geometry.

For all fragments, the velocity spectra are approximately Gaussian with a mean which decreases with increasing Z-value. This is the behavior expected for Coulomb-like velocities. For very light fragments, one also notices that the widths of the spectra become quite large. The first and second moments of the $V_e$ spectra were extracted for each Z-value and are plotted in Figs. 8 to 11.

The mean velocities display an almost linear decrease with increasing Z-value. A simple calculation of Coulomb velocities based on an initial scission-configuration of two spheres whose centers are separated by $1.2\times(A_1^{1/3}+A_2^{1/3})+2$ fm is shown by the dashed curves in Figs. 8 & 9. This parameterization was success-

ful in reproducing emission-velocities in lighter systems[5,8,27]. The calculation has also been corrected for sequential evaporation. The agreement between this simple calculation and the experimental data is quite good and confirms that the emission-velocities are Coulomb-like. Better agreement is possible if angular momentum effects are included in the calculations (Section 4.1.4).

The second moments of the experimental velocity distributions, shown in Figs. 10 & 11, decrease with increasing fragment charge. Changing the bombarding energy from E/A = 14.7 to 18.0 MeV resulted in only a small increase in these second moments. In contrast, a large increase was observed when the lighter C target was replaced by the heavier Al target. The widths of the velocity distributions arise both from fluctuations in the velocities of the primary fragments and from the recoil effects associated with the sequential evaporation of light particles from these fragments.

## 3.4 Angular Distributions and Cross Sections

The experimental angular distributions allow separation of the different complex fragment components. The $d\sigma/d\theta$ angular distributions in the frame of the source system were determined for all elements. Some representative examples are shown in Figs. 12 & 13. For the intermediate Z-values, $d\sigma/d\theta$ is constant and thus the fragment emission is symmetric about 180° in the center-of-mass, and has a $1/\sin\theta$ angular distribution corresponding to isotropic emission in the reaction plane. An "isotropic" component is also clearly visible for the lighter fragments, but at the backward angles $d\sigma/d\theta$ increases approximately exponentially. This exponential behavior is associated with the target-like component. Angular distributions similar to these have been observed both at lower[8,28-31] and at higher[10,32] bombarding energies.

For the $^{139}$La + $^{27}$Al reaction, the angular distributions become slightly forward peaked for the highest detected Z-values. Observe, for instance, the Z = 50 & 45 angular distributions in Fig. 13 for the E/A = 14.7 & 18.0 MeV reactions respectively. This forward peaking is associated with the projectile-like

deep-inelastic fragments. A similar feature has also been observed in previous studies[6,8].

For the $^{139}$La + $^{12}$C reactions, the shapes of the angular distributions are quantitatively very similar at the two measured bombarding energies. However, for the $^{139}$La + $^{27}$Al reactions there is a notable difference. Specifically, the angular distributions are constant over a much larger angular range at the lower bombarding energy. In Fig. 13, the d$\sigma$/d$\theta$ distributions for the E/A=14.7 MeV reaction are approximately constant for angles less than 130°. In comparison, the Z=4 & 5 angular distributions, for the E/A=18.0 MeV reaction, increase monotonically over the entire measured angular range. For this reaction, the deep-inelastic component is perhaps relatively more important at the higher bombarding energy. Similar conclusions were also drawn by Fields *et al.*[10] in the $^{14}$N + $^{nat}$Ag reaction.

As suggested by the form of the angular distributions, they were fitted with a constant plus an exponential term:

$$\frac{d\sigma}{d\theta} = C + K_1 e^{K_2\theta}. \tag{1}$$

The parameters C, $K_1$ and $K_2$ were adjusted, following the least squares method, to obtain the best fit to the experimental data. The resulting fitted curves are also shown in Figs. 12 & 13. These fits have been used to estimate the cross sections associated with the two components. The deep-inelastic cross section [$\sigma_{DI}$(Z)] was obtained by integrating over the exponential term in Eq. 1 and the isotropic cross section [$\sigma_{iso}$(Z)] was obtained from the constant term. The cross sections were calculated from the fitting parameters by:

$$\sigma_{DI} = \frac{K_1}{K_2}(e^{K_2\pi} - 1) \tag{2}$$

$$\sigma_{iso} = \pi C. \tag{3}$$

In Figs. 14 & 15, the extracted cross sections for each component are plotted as a function of the detected Z-value. Over the measured angular range, the constant-plus-exponential fitting function was found to adequately reproduce the

measured distributions. However, for any realistic angular distribution, $d\sigma/d\theta$ is expected to approach zero at $\theta = 0°$ and 180° and thus deviates from the constant-plus-exponential form. The cross sections extracted from the above equations should therefore overestimate the true values. For the isotropic component, this effect is not so important. At most, the cross sections are overestimated by 30%. For the target-like component, where most of the cross section in Eq. 2 originates from emission angles close to 180°, the effect could be larger. The largest possible error is a factor of 2 when the exponential component has the steepest slope. However, these considerations do not change the overall trends of the extracted charge distributions.

The shapes of the $\sigma_{iso}$(Z) distributions are all similar. They all display a peak at symmetric division associated with fission-like events. The cross sections for this component increase in value both with increasing excitation energy and target mass. The cross sections for the target-like component decrease very rapidly with increasing Z-value and extend out to larger Z-values for the reactions on the heavier Al target nuclei.

## 3.5 Coincidence Data

Events in which coincidence fragments were detected in two telescopes on opposite sides of the the beam axis were analyzed. Essentially no coincidences between telescopes on the same side of the beam axis were observed. This is consistent with the proposed binary nature of the complex fragment events. The $Z_1$-$Z_2$ correlation plots of the coincidence events are shown in Fig. 16. Here $Z_1$ and $Z_2$ refer to the Z-values of the particles detected in the two detectors. Most of the coincidence events lie in a band corresponding to an approximately constant sum of $Z_1$ and $Z_2$. This strongly emphasizes the binary nature of these events. The $Z_1+Z_2$ spectra for the two E/A=18 MeV reactions are shown in Fig. 17. The rather sharp peaks positioned near the total charge of the reaction again indicates the binary nature of these events.

The difference between the detected charge in the coincidence events and the

total charge of the reaction is the charge removed by light particle emission. This missing charge may be removed before the binary division or by sequential evaporation from the primary fragments. The mean missing charge:

$$< \Delta Z >= Z_{projectile} + Z_{target} - < Z_1 + Z_2 > \quad (4)$$

is plotted as a function of the charge of one of the fragments in Figs. 18 & 19. For the reactions on the $^{12}$C target, the charge loss is very small and similar in magnitude at the two bombarding energies. A small increase in the charge loss is observed for the more asymmetric coincidence events (events with small values of $Z_1$). For the reactions on the $^{27}$Al target, the charge loss is much larger and there are significant differences between the magnitude and asymmetry dependence of $< \Delta Z >$ at the two bombarding energies.

# 4 Discussion

The isotropic component of the complex fragments emitted in these reactions possesses many features which strongly suggests that it originates from the decay of a long-lived intermediate system (life-time $\gtrsim$rotational period). The questions which remain to be answered are:

1. Is the intermediate system formed in a complete or incomplete fusion process?

2. To what extent is this intermediate system fully equilibrated before it decays?

## 4.1 Isotropic Component in the $^{139}$La + $^{12}$C Reaction

### 4.1.1 Source Velocities

To answer the first question, one can examine the source velocities extracted from the Coulomb rings. The source velocity of an intermediate system produced by the complete amalgamation of the target and projectile fragments should be

identical to the center-of-mass velocity of the reaction ($V_{c.m.}$). For incomplete fusion, one expects only a fraction of the lighter, target nucleus to fuse with the heavier, projectile nucleus. The source velocity for such interactions would be larger than $V_{c.m.}$, but less than the beam velocity ($V_{beam}$). An accurate determination of $V_{source}$ should allow one to infer the degree of fusion. Unfortunately in this work, the extracted source velocities have a possibly large systematic error ($\pm 0.04 \times V_{beam}$) compared to the range of possible source velocities (0.92 to $1.00 \times V_{beam}$), making such a determination uncertain. However, one can look for a difference between the relative degrees of fusion at the two bombarding energies. In Fig. 3, the experimental ratios of $V_{source}/V_{beam}$ for both bombarding energies are almost identical, although at the higher bombarding energy, the ratio is slightly larger by 0.5 to 1% for all Z species. This could easily be attributed to systematic errors, so $V_{source}/V_{beam}$ is identical to within 1% at the two bombarding energies. This implies that, on average, at the two bombarding energies the same number of target nucleons, to within 0.7 nucleons, fuse with the projectile nucleus.

The independence of $V_{source}/V_{beam}$ on the bombarding energy was also observed in the $^{93}$Nb + $^{9}$Be & $^{12}$C reactions over a larger range of E/A (11.4 to 18.0 MeV)[6]. This was taken as evidence that, for these reactions, complex fragments were produced predominantly in complete fusion processes. Although at such bombarding energies, both complete and incomplete fusion reactions are expected to occur, complex fragments may select out preferentially the complete fusion component, i.e. compound nuclei formed in incomplete fusion reactions will have reduced excitation energies and angular momenta relative to those formed in complete fusion. Owing to the large dependence of the decay probabilities on these two quantities, complex fragments may be associated predominantly with the complete fusion reactions[5]. By analogy, the same is believed true for the $^{139}$La + $^{12}$C reactions of this work.

### 4.1.2 Cross Sections

To address the second question concerning the degree of equilibration of the intermediate systems, one needs to compare the experimental data to the predictions of the statistical model. To this end, statistical model calculations were performed with the Monte Carlo computer code GEMINI[6]. This code simulates the decay of a compound nucleus via a series of binary decays. All possible binary divisions of the system from light particle emission to symmetric fission are allowed at each decay step. After each binary division, the decay of the resulting fragments is followed until all the available excitation energy is exhausted. The decay-widths for light particle emission ($Z \leq 2$) were calculated with the Hauser-Feshbach formalism[33], while the decay-widths for the other binary decays were calculated from the transition-state formalism[12]. In the transition-state formalism, the decay-widths are very sensitive to the conditional saddle-point energies as a function of mass-asymmetry and angular momentum. The conditional saddle-point energies used in the simulations were calculated by Carjan and Alexander[34] with the RFRM[24].

The CN spin distribution was assumed to have the form:

$$\sigma(\ell) = \pi \lambda\!\!\!^{-2}(2\ell+1)\frac{1}{1+e^{\frac{\ell-\ell_0}{\delta}}}. \qquad (5)$$

The diffuseness parameter $\delta$ was set to a value of 4 $\hbar$ for both bombarding energies. This value is similar to those needed to fit experimental fission excitation functions at low bombarding energies[35,36]. In contrast, at these higher bombarding energies, the results of the statistical model calculations were found to be quite insensitive to the exact value of $\delta$. The parameter $\ell_0$ was adjusted so that the simulations reproduced the experimental "fission" cross section, i.e. the cross section associated with the peak in the charge distributions centered at symmetric division. The resulting values of $\ell_0$ obtained by this procedure are 55 and 58 $\hbar$ for E/A = 14.7 & 18.0 MeV $^{139}$La + $^{12}$C reactions, respectively. In comparison, the 1977 Bass Model[37] predictions are 68 and 76 $\hbar$ respectively, which are much larger than these fitted values. However, at such high angular momenta,

the effective fissility of the system is increased and extra-push effects may become important. The values of $\ell_0$ predicted by the extra-push model[38,39] are 59 and 61 $\hbar$, respectively. These are in much better agreement with the fitted values.

The predicted charge distributions are compared with the experimental data in Fig. 20. The agreement is good, thus the experimental charge distributions can be adequately reproduced by the statistical model. This is the strongest evidence for the formation of compound nuclei in these reactions. One should note that complex fragment emission is still a relatively rare occurrence. Most of the compound systems formed in these $^{139}$La + $^{12}$C reactions decay only by light particle emission. Thus, the majority of the predicted yield falls in the evaporation residue peak. This peak is associated predominantly with "classical evaporation residues", which result from systems that decay only via the evaporation of $Z \leq 2$ particles. The predicted cross sections for "classical evaporation residues" are indicated by the dashed histograms in Fig. 20 and the total cross section for these events account for $\approx$85% of the initial fusion cross section in the simulations. At the other extreme, the predicted cross section for ternary and higher order complex fragment events is very small, $\approx$1 mb at both bombarding energies. Apart from these very rare events, the simulated yield for $3<Z<50$ is associated with binary complex fragment events.

One interesting comparison between the predicted and measured charge distributions is that the predicted fission-peak is broader than that observed experimentally. It is possible that the RFRM conditional barriers need to be modified slightly. Only small changes in the mass-asymmetry dependence of the conditional barriers are required to produce large charges in the shape of the predicted charge distributions. As an example, one could reproduce the shape of the experimental charge distribution by lowering the height of the minimum in the conditional barriers at symmetry by $\approx$2 MeV or alternatively by increasing the height of the maximum at intermediate asymmetries by the same amount. Of course there are many other parameters in the statistical model whose values are not well known. Adjustment of these parameters, especially as a function

of mass-asymmetry, may also allow one to obtain better agreement with the data. However, an arbitrary adjustment of parameters will not lead to a better understanding of CN decay.

Another possibility is that the narrowing of the fission-peak is a dynamical effect. The transition-state formalism predicts the probability distribution along the saddle-point ridge-line in the potential energy landscape. For very light systems, the saddle- and scission-points are almost degenerate so that the saddle-point populations are preserved at scission. However, as the decaying system becomes more fissile, the descent from saddle to scission for symmetric divisions becomes longer. Thus, there exists the possibility of a dynamical rearrangement of the saddle-point populations during this descent. Specifically for the systems in this study, the potential energy is a minimum for symmetric division so the driving force is towards symmetry, which may result in a narrowing of the fission-peak. However, the magnitude of the effect is not known at present. Further dynamical calculations are necessary to clarify this point.

### 4.1.3 Missing Charge

The GEMINI simulations were also used to predict the missing charge measured in the coincidence measurements. This charge includes the charge lost due to light particle evaporation from the CN prior to scission and from the primary fragments after scission. In order to estimate the post-scission evaporated charge, one needs to know the excitation energy and spin of the excited primary fragments. In previous GEMINI calculations[6,8], the thermal excitation energy at the saddle-point was assumed to be divided between the nascent fragments in proportion to their masses (equal temperatures). In this work, the calculations were extended to also include thermal fluctuations in the partition of excitation energy: the thermal excitation energy of one fragment ($U_1$) has the probability distribution function[40]

$$p(U_1) \propto \rho_1(U_1)\,\rho_2(U_{sad} - U_1) \tag{6}$$

where $U_{sad}$ is the total thermal excitation energy at the saddle-point. The level densities of the two fragments $\rho_1, \rho_2$ were assumed to have Fermi-gas dependences. Except for very asymmetric divisions, this distribution function is well approximated by a gaussian form[40] with a mean corresponding to a sharing of the excitation energy according to equal temperatures and a variance of

$$\sigma^2(T) = 2T^3 \frac{a_1 a_2}{a_1 + a_2} \tag{7}$$

where $a_1$ and $a_2$ are the Fermi-gas level density parameters for the two fragments and T is the temperature at the saddle-point.

For rigid rotation of the saddle-point configuration, the total angular momentum of the CN is partitioned between the spins of the nascent fragments and the orbital motion in proportion to their respective moments of inertia. In the simulations, fluctuations in these values due to the excitation of the angular-momentum-bearing collective modes[41,42]: twisting, bending, wriggling, tilting, were included.

The inclusion of spin and excitation energy fluctuations did not affect the predicted post-scission evaporated charge. The largest effect was obtained for the very asymmetric divisions. The calculated and experimental mean missing charges are plotted in Fig. 18 as a function of the Z-value of one of the coincidence fragments. The contribution to the predicted missing charge from pre-scission evaporation was calculated to be small, approximately 0.1 for all asymmetries.

The effects of the detector geometry and the experimental thresholds on the observed missing charge were also investigated. The simulated angular and velocity distributions of the emitted fragments are discussed later (Section 4.1.4). The predicted mean missing charge for "detected" coincidence events is indicated by the dashed curves in Fig. 18. Except for very asymmetric divisions, the predictions do not differ (to within the statistics of the simulations) from the original calculations without the detector filter.

The agreement between the predicted and observed missing charge in Fig. 18 is reasonable allowing for the experimental error ($\pm 1$). The increase in the missing charge for the more asymmetric divisions arises, in the simulations, from the fact

that the lighter fragment emits more charged particles per MeV of excitation energy.

### 4.1.4 Emission-Velocity Spectra

The finite widths of the measured emission-velocity distributions are thought to arise largely from the recoil effects associated with the evaporation of light fragments from the hot primary fragments. Other processes also contribute to the magnitude of these widths, i.e.: light particle emission from the CN before scission; fluctuations in the both Coulomb barrier and the orbital angular momentum at scission; and the detector resolution.

The effects of evaporation have been included in the GEMINI simulations. The angular distributions of all emitted particles were calculated from Ref. 42 taking into account the collective modes. For the emission of heavy fragments there are 6 normal angular-momentum-bearing modes which can be excited whereas for light particle emission only 3 modes are possible. The kinetic energy of the emitted particles was calculated as:

$$E_k = E_{Coul} + E_{sep} + \frac{\ell^2 \hbar^2}{2\mu R^2} \tag{8}$$

where the Coulomb energy was calculated from the parameterization of Section 3.3. No fluctuations in the Coulomb energy were included in the calculations. The kinetic energy associated with the separation degree-of-freedom at scission ($E_{sep}$) was set to its average value (T). Fluctuations in this quantity were not considered. The last component of $E_k$ in Eq. 8 arises from the orbital angular momentum of the two nascent fragments. The magnitude of the orbital angular momentum ($\ell$) in the simulations includes fluctuations resulting from the excitation of the various collective angular-momentum-bearing modes. The quantity $\mu$ is the reduced mass. For light particle emission from a system with zero total angular momentum, the average value of the orbital component of $E_k$ is also T, and thus the average value of $E_k$ reduces to the well known form:

$$E_k = E_{Coul} + 2T. \tag{9}$$

The simulated first and second moments of the velocity distributions are compared to the experimental data in Figs. 8 & 10. The mean velocities are well reproduced by the simulations. As discussed previously, the emission-velocities of the fragments arise predominantly from the Coulomb repulsion between the nascent fragments, as indicated by the dashed curves in the Fig. 8. There is a small increase in the predicted velocities due to the inclusion of the energy associated with the orbital angular momentum. However, the simulations may not accurately predict the magnitude of this component as they ignore the dependence of the deformation of the saddle-point configuration on the CN spin. Larger deformations decrease the Coulomb energy and increase the orbital energy. To predict the mean velocities more accurately, one should consider this effect plus the motion of the system during the descent from the saddle- to the scission-point.

The second moments predicted by the simulations arise predominantly from the recoil effects associated with post-scission light particle evaporation. The contributions from pre-scission evaporation and the angular momentum fluctuations were found to be small. The experimental widths are well reproduced by the calculations especially for the heavier fragments. The experimental widths should also include a component arising from our imprecise method of determining the fragment velocities (see Section 3.1). This was also simulated in the GEMINI calculations and the resulting velocity widths increased slightly. This is illustrated by the dashed curves in Fig. 10. Even when this effect is included, the agreement with the experimental data is still good.

The statistical model simulations using the RFRM conditional barriers are able to reproduce the experimental cross sections, the widths of the emission-velocity distributions and the missing charge observed in coincidence events. Thus, the isotropic component of complex fragments in the $^{139}$La + $^{12}$C reactions are entirely consistent with the statistical decay of compound nuclei formed in complete fusion reactions, although one cannot rule out a small amount of incomplete fusion. These conclusions are similar to those obtained in our

investigations[6,8] of $^{93}$Nb & $^{63}$Cu + $^{12}$C reactions at comparable bombarding energies.

## 4.2 Isotropic Component in the $^{139}$La + $^{27}$Al Reaction

### 4.2.1 Cross Sections

The isotropic complex fragment component in the $^{139}$La + $^{27}$Al reactions is also associated with the decay of long lived intermediate systems, but unlike the $^{139}$La + $^{12}$C reaction, the majority of these fragments cannot be produced by the **statistical decay** of compound nuclei formed in **complete fusion** reactions. This is most clearly illustrated in Fig. 21, where statistical model calculations of the fragment cross sections are compared to the experimental data. These calculations were performed for compound nuclei formed in complete fusion reactions with spin distributions given by Eq. 5. The parameter $\delta$ was set to a value of 0 $\hbar$ and the parameter $\ell_0$ was increased to the value $\ell_{B_f=0}$ = 82 $\hbar$, the largest CN spin for which there is still a barrier against symmetric division. The barriers for larger asymmetries also vanish at higher angular momenta. Therefore, for spins above $\ell_{B_f=0}$, a CN cannot be formed. The shapes of the experimental $\sigma$(Z) distributions are well reproduced by the calculations in Fig. 21. However, the experimental yields for all Z-values are substantially underestimated, implying that $\ell$-waves of angular momentum greater than $\ell_{B_f=0}$ must also be associated with the isotropic component. Similar conclusions were also obtained for the $^{93}$Nb + $^{27}$Al and $^{63}$Cu + $^{27}$Al reactions of Refs. 6 & 8.

The need for such large values of $\ell_0$ can be deduced from the total fragment cross sections without resorting to statistical model calculations. Table 1 lists the total cross sections $\sigma(4 \leq Z \leq Z_{sym})$ associated with isotropic fragment emission ($Z \geq 4$) for various reactions on $^{27}$Al targets. To reproduce such cross sections, the maximum $\ell$-wave associated with the isotropic component must have values greater than

$$\ell_a = \sqrt{\frac{\sigma(4 \leq Z \leq Z_{sym})}{\pi \lambda^2}} - 1. \qquad (10)$$

The quantity $\ell_a$ gives only a lower limit to the maximum $\ell$-wave associated with

the isotropic component, as the cross section for evaporation residues has been ignored. This cross section has been estimated from the GEMINI simulations and when added to the total complex fragment cross sections, a better estimate ($\ell_b$) of the maximum $\ell$-wave is obtained. In the reactions on the $^{27}$Al target, unlike those on the $^{12}$C target, the evaporation residue cross sections are much smaller than the total complex fragment cross sections and thus $\ell_b$ is only slightly larger than $\ell_a$. The derived values of $\ell_a$ and $\ell_b$ are compared to the predicted values of $\ell_{B_f=0}$[24] in Table 1. In all cases, $\ell$-waves of angular momentum greater than $\ell_{B_f=0}$ are necessary to explain the large cross sections for the isotropic component.

This experimental observation may have the following explanations:

1. Because of the large temperatures induced in these reactions (T=4-5.5 MeV), the conditional barriers are lower than those calculated for cold nuclei.

2. The values of $\ell_{B_f=0}$ predicted by the RFRM are too low.

3. Light particle emission during the fusion dynamics reduces the spin of the resulting CN to a value below $\ell_{B_f=0}$. This emission may be either pre-equilibrium or statistical.

4. For collisions with $\ell > \ell_{B_f=0}$, the reaction proceeds via the fast-fission mechanism.

Numerous theoretical studies have addressed the question of the temperature dependence of the potential energy surface[43-47]. Such studies have usually investigated the lowering of the symmetric fission barrier with increasing nuclear temperature. Of course, all conditional barriers should decrease with increasing temperature although the dependence may vary with mass-asymmetry. The introduction of temperature-dependent conditional barriers in the simulations would probably increase the predicted complex fragment cross sections, but one would still **not** be able to reproduce the experimental data. The reason for this is: a finite temperature is also predicted to lower the value of $\ell_{B_f=0}$[48] and from

the above discussion, we have already concluded that $\ell$-waves with angular momentum larger than the value of $\ell_{B_f=0}$ for cold nuclei are required to reproduce the observed cross sections.

Although the magnitude of $\ell_{B_f=0}$ has not been determined experimentally, there is no reason to believe the RFRM predictions are incorrect by up to 40 or 50 $\hbar$. Certainly, barriers predicted by the RFRM, when used in statistical model calculations, are able to reasonably reproduce the charge distributions of complex fragments emitted from systems at high angular momentum ($\ell_0$=70 $\hbar$[26]). This gives confidence in the use of the RFRM model at these high angular momenta. The more simplistic Rotating-Liquid-Drop Model (RLDM) predicts values of $\ell_{B_f=0}$ approximately 10 $\hbar$ larger than the RFRM for the systems of interest. With such values, one might conclude from Table 1 that the E/A = 14.7 MeV $^{139}$La + $^{27}$Al reaction could be associated with statistical decay following complete fusion. However, the other reactions in Table 1 would still not be consistent with this mechanism.

At lower bombarding energies, the production of fission fragments via fast-fission reactions where $\ell_0 > \ell_{B_f=0}$ is well documented[49-51]. In such reactions, the system is believed to be trapped behind the mass-asymmetric barrier at the entrance-channel asymmetry, but after mass-equilibration occurs, it then escapes. Although these reactions do not proceed through the CN stage, they present many features which are typical of CN fission, i.e. Coulomb-like velocities, and in some cases, $1/\sin\theta$ angular distributions ($d\sigma/d\Omega$). The fast-fission mechanism has already been suggested[52] to explain some features of the charge distribution of the fragments detected in the similar reaction $^{82}$Kr + $^{27}$Al at a much lower bombarding energy (E/A=5.9 MeV). Such a reaction mechanism may also be consistent with the $^{27}$Al data of this work. The charge distributions are expected to be determined largely by the potential energy surface at the closest approach of the two interacting fragments[53]. Certainly, the shapes of the charge distributions in this work qualitatively reflect the asymmetry dependence of the potential energy surface. In fact, for all the reactions listed in Table 1, the

statistical model calculations were found to reproduce the correct shape, though not the magnitude, of the measured charge distributions. Further calculations are necessary to determine whether the data is quantitatively consistent with the fast-fission mechanism.

In fusion or fast-fission reactions, the emission of light fragments at an early stage in the interaction may account for a large fraction of the total angular momentum. In such a scenario, CN formation could still be possible for collisions with $\ell > \ell_{B_f=0}$, if sufficient angular momentum is removed by these light fragments. Certainly at the higher bombarding energies, some amount of incomplete-fusion or pre-equilibrium emission of light particles is expected. Also, one cannot rule out statistical emission of such fragments during the dynamics of a fusion-like interaction. If the excitation energy is dissipated early in the reaction, then statistical emission of light particles may be possible while the gross collective degrees-of-freedom are still governed by the fusion dynamics. At the excitation energies corresponding to complete fusion in the reactions on $^{27}$Al, the decay time for light particle emission is $\approx 1\times10^{-21}$ s. This is of the same order as the pre-scission lifetime for such systems[54].

### 4.2.2 Source Velocities

Evidence for some role of incomplete fusion in these complex fragment events is found in the extracted source velocities. In Fig. 3, the experimental ratios $V_{source}/V_{beam}$, for Z-values associated with symmetric division, show a dependence on the bombarding energy which is probably significant. If this is correct, it implies that for E/A=18.0 MeV, symmetric division is associated, on average, with some degree of incomplete fusion. However, because of the possibly large systematic error in these measurements, one cannot determine the exact degree of fusion but only that, at the higher bombarding energy, less of the target nucleus is absorbed by the projectile. Thus, it is impossible to judge whether the E/A=14.7 MeV reaction is associated with complete or incomplete fusion. The difference between the two measured values of $V_{source}/V_{beam}$ for symmetric divi-

sion is 0.016±0.008. This would be consistent with, on average, ≈3 more target nucleons escaping fusion with the projectile at the higher bombarding energy. However, for the more asymmetric divisions, no difference in $V_{source}/V_{beam}$ is observed between the two bombarding energies. This may be understood in terms of the statistical emission hypothesis: for incomplete fusion reactions, a distribution in the number of target nucleons absorbed by the projectile is expected giving rise to a distribution of CN velocities. Also, the emission probability for heavy fragments increases very rapidly with both increasing excitation energy and angular momentum. Thus, on average, complex fragments will be emitted in interactions with the highest degree of fusion, which correspond to the largest CN excitation energies and spins and to the slowest source velocities. Now, the increase in the emission probability with excitation energy and spin is largest for binary divisions with the largest barriers and hence, the lowest yields. Thus, the mean source velocity is weighted towards the lowest possible values for these fragments. Therefore, variations in the mean source velocity should correlate with variations in corresponding fragment yields. This is the case for the E/A=18 MeV reaction. However, for the E/A=14 MeV reaction there is little or no variation in the source velocities for different fragment Z-values. This suggests that the initial distribution of the CN velocities must be narrower for the reaction at the lower bombarding energy. However, because of the large systematic error one should be careful about drawing too strong a conclusion. More accurate measurements of the source velocities are necessary to determine the role of incomplete fusion, if any, in these reactions.

One should also note that in the $^{93}$Nb + $^{27}$Al reactions, no dependence of the extracted ratios $V_{source}/V_{beam}$ was observed over an even larger range of bombarding energies (E/A = 11.4 to 18.0 MeV)[6]. Thus, there is no evidence that incomplete fusion reactions are associated with the complex fragments emitted in the $^{93}$Nb + $^{27}$Al reaction. Fast-fission may be the more important production mechanism of complex fragments in this reaction. In the $^{139}$La + $^{27}$Al reaction, possibly some combination of both fast-fission and incomplete fusion or

pre-equilibrium emission processes may be associated with most of the isotropic component. For lower $\ell$-waves, statistical emission is probably still important.

### 4.2.3 Missing Charge and Emission-Velocity Spectra

The calculated missing charge and the moments of the velocity distributions are also compared to the experimental data in Figs. 9, 11 & 19. In the simulations both the missing charge and the second moment of the velocity distributions were determined predominantly by the sequential evaporation of light particles from the primary fragments. Although the simulations may not treat the decay process correctly for these reactions, if a large fraction of the available excitation energy is deposited into the primary fragments, these simulated quantities should be meaningful. The experimental values of $\sigma(V_e)$ are significantly larger than the calculation and thus the major source of the velocity fluctuations is not sequential evaporation. A similar conclusion was obtained for the complex fragments emitted in the reactions Nb + Al at E/A = 25 and 30 MeV[5]. Another possible source may arise from a distribution of source velocities associated with incomplete fusion. Alternatively, the fluctuations in the Coulomb energy of the two nascent fragments may be significantly larger in these reactions.

The statistical model calculations do not reproduce the missing charge associated with the coincidence events. Some of the coincidence events detected in these reactions may arise from the deep-inelastic component as this component has appreciable cross section for fragments of $Z \leq 12$. However, if one considers only the more symmetric decays, there is still a disagreement between the calculation and the experimental data. Therefore, charge losses from mechanisms other than sequential evaporation must be important. Also, the reason why the dependence of $< \Delta Z >$ on $Z_1$ is different for the two bombarding energies is not clear (see Fig. 19).

## 4.3 Target- and Projectile-like Components

In considering the origins of the target- and projectile-like components, it is useful to compare the results of this work with those obtained in similar reactions at higher and at lower bombarding energies. The complex fragment angular distributions of this work are very similar to those measured in the reaction $^{19}F+^{89}Y$ at the much lower bombarding energy E/A=7 MeV (see Fig. 14 of Ref. 28). The $d\sigma/d\theta$ distributions measured in the $^{19}F+^{89}Y$ reaction can also be decomposed into isotropic and "exponential" components. The isotropic component was claimed to be associated with deep-inelastic reactions in Ref. 28, though its magnitude is also consistent with compound nucleus emission[55]. The "exponential" component corresponds to incompletely damped interactions and is typical of what one expects for quasi- and deep-inelastic reactions. Similar results have been measured for other reactions at E/A$\approx$10 MeV[29-31].

The "exponential" component in this work, differs from that found at the lower energies in that $\sigma$(Z) is no longer peaked near the Z-value of the target (or projectile for normal kinematics reactions). This is typical of the charge distributions of light complex fragments emitted in reactions at E/A>20 MeV, where $\sigma$(Z) has a maximum for protons and decreases with an approximate power law dependence[1,56-58]. At these higher energies, complex fragment emission is essentially still a binary process[1,14] though it has not always been associated with deep-inelastic interactions. However, there seems to be a continuous evolution of this component from low bombarding energies (E/A<10 MeV) to the higher energies. Compare for example the studies of complex fragment emission in the $^{14}N + ^{nat}Ag$ reaction of Moretto *et al.*[30] from E/A = 7.1 to 17.9 MeV and of Fields *et al.*[10] from E/A = 20 to 60 MeV. However, the reaction mechanisms at the high and low bombarding energies may not be identical. Low bombarding energies are best described in terms of the mean field whereas, at the higher bombarding energies, nucleon-nucleon collisions should also be included.

# 5 Summary

Complex fragments were detected in the reactions $^{139}$La + $^{12}$C & $^{27}$Al at the bombarding energies of E/A = 14.7 and 18.0 MeV. From the measured angular and velocity distributions, the observed complex fragment emission could be separated into two components. A component associated with the binary decay of a long-lived intermediate system, which has an isotropic angular distribution in the reaction plane and a deep-inelastic component. The latter component comprises both projectile- and target-like fragments.

The isotropic component in the $^{139}$La + $^{12}$C reactions was found to result from the statistical binary decay of CN formed in complete fusion reactions, although a very small degree of incomplete fusion could not be excluded. The experimental cross sections, velocity distributions, and the missing charge associated with coincidence events were all well reproduced by statistical model simulations. The latter two quantities were found to result predominantly from the sequential emission of light particles from the primary fragments. Within the uncertainty of the other statistical model parameters, the Rotating-Finite-Range Model conditional barriers were found to be consistent with the experimental charge distributions when realistic CN spin distributions were assumed.

In the $^{139}$La + $^{27}$Al reactions, the isotropic component was found to be associated with $\ell$-waves of angular momentum larger than the maximum value for which CN formation is still possible in complete fusion reactions. There was some suggestion that, at least at the higher bombarding energy, the fragments may be associated with incomplete fusion reactions. It was speculated that, if sufficient angular momentum was removed by such processes, a CN could still form and emit fragments statistically. Alternatively, the appropriate reaction mechanism may be fast-fission. More accurate measurements of the fragment's source velocities are necessary to accurately gauge the importance of incomplete fusion and/or fast-fission in this reaction.

## *Acknowledgement

This work was supported by the Director, Office of Energy Research, Office of High Energy and Nuclear Physics, Nuclear Physics Division of the U. S. Department of Energy, under contract DE-AC03-76SF00098.

| Reaction | E/A MeV | $\sigma(4 \leq Z \leq Z_{sym})$ mb | $\ell_a$ $\hbar$ | $\ell_b$ $\hbar$ | $\ell_{B_f=0}$ $\hbar$ |
|---|---|---|---|---|---|
| $^{63}$Cu + $^{27}$Al | 12.6 | 1300 ± 260 | 94 ± 9 | 106 | 71 |
| $^{93}$Nb + $^{27}$Al | 11.4 | 1100 ± 220 | 90 ± 8 | 105 | 78 |
| | 14.7 | 1485 ± 300 | 120± 11 | 131 | |
| | 18.0 | 1800 ± 360 | 146± 14 | 155 | |
| $^{139}$La + $^{27}$Al | 14.7 | 548 ± 120 | 79 ± 8 | 95 | 82 |
| | 18.0 | 870 ± 200 | 110 ± 12 | 118 | |

Table 1 Angle-integrated cross sections $\sigma(4 \leq Z \leq Z_{sym})$ associated with the isotropic emission of fragments ($Z \geq 4$) in various reactions on $^{27}$Al targets (from this work and from Refs. 6 & 8). The quantities $\ell_a$ indicates the maximum $\ell$-wave required to reproduce these cross sections. When the evaporation residue cross sections predicted by GEMINI are added to $\sigma(4 \leq Z \leq Z_{sym})$, the maximum $\ell$-wave needed reproduce this cross section is given by $\ell_b$. Compare these values to the predicted angular momentum $\ell_{B_f=0}$ at which the symmetric fission barrier of the CN first vanishes[24].

Fig. 1 Representative contour plots of the experimental cross section $\partial^2\sigma/\partial V_{\|}\partial V_{\perp}$ in the $V_{\|}$-$V_{\perp}$ plane for fragments detected in the reaction E/A=18.0 MeV $^{139}$La + $^{12}$C. The beam direction is vertical. The dashed lines indicate the angular and low-velocity thresholds due to detector properties.

Fig. 2 Same as in Fig. 1, for the reaction E/A=18.0 MeV $^{139}$La + $^{27}$Al.

Fig. 3 Source velocities extracted from the Coulomb rings as a function of the fragment Z-value. The small error bar on each point represents the statistical error associated with the extraction process. The larger error bar, for each data set, indicates the possible systematic error. The center-of-mass velocities for the two reactions are shown by the dotted lines. Note the suppressed zero on the ordinate.

Fig. 4 Experimental emission-velocity spectra for boron (Z=5) fragments emitted in the reaction E/A=18.0 MeV $^{139}$La + $^{12}$C. The emission angle in the frame of the source system is indicated for each spectrum.

Fig. 5 Same as in Fig. 4, for the reaction E/A=18.0 MeV $^{139}$La + $^{27}$Al.

Fig. 6 Representative emission-velocity spectra for the isotropic complex fragment component measured in the E/A=18.0 MeV $^{139}$La + $^{12}$C reaction.

Fig. 7 Same as in Fig. 6, for the reaction E/A=18.0 MeV $^{139}$La + $^{27}$Al.

Fig. 8 Mean emission-velocities for the isotropic component measured as a function of the fragment Z-value in the reaction E/A = 14.7 & 18.0 MeV $^{139}$La + $^{12}$C. The dashed curves show the result of a simple calculation where the emission-velocity arises solely from the Coulomb repulsion at scission. The velocities predicted by the GEMINI code which also includes the contribution from the orbital angular momentum are indicated by the solid curves (see text).

Fig. 9 Same as in Fig. 8, for the $^{139}$La + $^{27}$Al reaction.

Fig. 10 Second moments of the emission-velocity spectra for the isotropic component measured as a function of the fragment Z-value in the reaction E/A=14.7 & 18.0 MeV $^{139}$La + $^{12}$C. The solid curves show the predictions of the GEMINI code. The dashed curves indicate the predicted second moments when the experimental resolution arising from the method of estimating velocity is also included in the GEMINI simulations.

Fig. 11 Same as in Fig. 10, for the $^{139}$La + $^{27}$Al reaction.

Fig. 12 Representative $d\sigma/d\theta$ angular distributions in the frame of the source system for the E/A=14.7 & 18.0 MeV $^{139}$La + $^{12}$C reactions. The Z-value and normalization factor are shown to the left and right, respectively, of each angular distribution. The solid curves show fits to the experimental data (see text).

Fig. 13 Same as in Fig. 12, for the $^{139}$La + $^{27}$Al reaction.

Fig. 14 Angle-integrated cross sections for both the isotropic (open circles) and deep-inelastic (solid circles) components measured as a function of the fragment Z-value in the $^{139}$La + $^{12}$C reaction.

Fig. 15 Same as in Fig. 14, for the $^{139}$La + $^{27}$Al reaction.

Fig. 16 Contour plots of the charge correlation for detected coincidence events. $Z_1$ and $Z_2$ refer to the Z-values of the fragments detected in the two telescope arrays on either side of the beam axis. The contour scale is logarithmic with neighboring contours differing in value by a factor of 3. For reference, coincidence events where $Z_1+Z_2$ equals the total charge in the reaction should fall along the dashed curves. The extension of some contours above this line is an artifact of the imperfect detector Z-resolution. Because of the logarithmic scale, this effect is magnified in these plots.

Fig. 17 The relative yield of coincidence events plotted as a function of the sum of the atomic charges of the coincident fragments in the E/A = 18 MeV reactions.

Fig. 18 The average missing charge associated with coincidence events detected in the reactions $^{139}$La + $^{12}$C plotted as a function of the charge detected in one of the detectors. The error bar indicates the possible systematic error due to the uncertainties in the Z-value identification. The solid and dashed curves show the missing charge predicted with the GEMINI simulations for all events and for "detected" coincidence events (the detector geometry and thresholds were included in the simulations), respectively.

Fig. 19 Same as for Fig. 18, for the $^{139}$La + $^{27}$Al reaction.

Fig. 20 Comparison between the experimental (data points) and predicted (histogram) charge distributions for the isotropic component of complex fragments emitted in the E/A=14.7 & 18.0 MeV $^{139}$La + $^{12}$C reaction. The excitation energies and spin distribution parameters

used in the GEMINI calculations are indicated. The dashed histograms show the cross section associated with "classical evaporation residues" which decay only by the emission of light particles ($Z \leq 2$).

Fig. 21 Same as in Fig. 20, for the $^{139}La + ^{27}Al$ reaction.

# References


[1] D.J. Fields, W.G. Lynch, T.K. Nayak, M.B. Tsang, C.B. Chitwood, C.K. Gelbke, R. Morse, J. Wilczynski, T.C. Awes, R.L. Ferguson, F. Plasil, F.E. Obenshain, and G.R. Young, Phys. Rev. **C34** (1986) 536.

[2] K. Kwiatkowski, J. Bashkin, H. Karwowski, M. Fatyga, and V.E. Viola, Phys. Letts. **B171** (1986) 41.

[3] M. Fatyga, K. Kwiatkowski, V.E. Viola, W.G. Wilson, M.B. Tsang, J. Pochodzalla, W.G. Lynch, C.K. Gelbke, D.J. Fields, C.B. Chitwood, Z. Chen, and T. Nayak, Phys. Rev. Letts. **58** (1987) 2527.

[4] T. Kozik, J. Buschmann, K. Grotowski, H.J. Gils, H. Heide, J. Kiener, H. Klewe-Nebenius, H. Rebel, S. Zagromski, A.J. Cole, and S. Micek, Z. Phys. **A326** (1987) 421.

[5] R.J. Charity, D.R. Bowman, Z.H. Liu, R.J. McDonald, M.A. McMahan, G.J. Wozniak, L.G. Moretto, S. Bradley, W.L. Kehoe, and A.C. Mignerey, Nucl. Phys. **A476** (1988) 516.

[6] R.J. Charity, M.A. McMahan, G.J. Wozniak, R.J. McDonald, L.G. Moretto, D.G. Sarantites, L.G. Sobotka, G. Guarino, A. Pantaleo, L. Fiore, A. Gobbi, and K.D. Hildenbrand, Nucl. Phys. **A483** (1988) 371.

[7] D.R. Bowman, W.L. Kehoe, R.J. Charity, M.A. McMahan, A. Moroni, A. Bracco, S. Bradley, I. Iori, R.J. McDonald, A.C. Mignerey, L.G. Moretto, M.N. Namboodiri, and G.J. Wozniak, Phys. Letts. **B189** (1987) 282.

[8] H.Y. Han, K.X. Jing, E. Plagnol, D.R. Bowman, R.J. Charity, L. Vinet, G.J. Wozniak, and L.G. Moretto, Nucl. Phys. **A492** (1989) 138.

[9] E. Plagnol, L. Vinet, D.R Bowman, Y.D. Chan, R.J. Charity, E. Chavez, S.B. Gazes, H. Han, W.L. Kehoe, M.A. McMahan, L.G. Moretto, R.G. Stokstad, G.J. Wozniak, and G. Auger, Phys. Letts. **B221** (1989) 11.

[10] D.E. Fields, K. Kwiatkowski, D. Bonser, R.W. Viola, V.E. Viola, W.G. Lynch, J. Pochodzalla, M.B. Tsang, C.K. Gelbke, D.J. Fields, and S.M. Austin, Phys. Letts. **B220** (1989) 356.

[11] K. Grotowski, J. Ilnicki, T. Kozik, J. Łukasik, S. Micek, Z. Sosin, A. Wieloch, N. Heide, H. Jelitto, I. Kiener, H. Rebel, S. Zagromski, and A.J. Cole, Phys. Letts. **B223** (1989) 287.

[12] L.G. Moretto, Nucl. Phys. **A247** (1975) 211.

[13] Ch. Egelhaaf, M. Bürgel, H. Fuchs, A. Gamp, H. Homeyer, D. Kovar, and W. Rauch, Nucl. Phys. **A405** (1983) 397.

[14] B. Borderie, M.F. Rivet, C. Cabot, D. Fabris, D. Gardès, H. Gauvin, F. Hanappe, and J. Péter, Z. Phys. **A318** (1984) 315.

[15] B. Borderie, M. Montoya, M.F. Rivet, D. Jouan, C. Cabot, H. Fuchs, D. Gardès, H. Gauvin, D. Jacquet, F. Monnet, and F. Hanappe, Phys. Letts. **B205** (1988) 26.

[16] U.L. Businaro and S. Gallone, Nuovo Cim. **1** (1955) 629.

[17] M. Beckerman and M. Blann, Phys. Rev. **C17** (1978) 1615.

[18] M. Blann and T.T. Komoto, Phys. Rev. **C26** (1982) 472.

[19] B. Sikora, W. Scobel, M. Beckerman, J. Bisplinghoff, and M. Blann, Phys. Rev. **C25** (1982) 1446.

[20] G. Guillaume, J.P. Coffin, F. Rami, P. Engelstein, B. Heusch, P. Wagner, P. Fintz, J. Barrette, and H.E. Wegner, Phys. Rev. **C26** (1982) 2458.

[21] D.J. Hinde, J.R. Leigh, J.O. Newton, W. Galster, and S. Sie, Nucl. Phys. **A385** (1982) 109.

[22] D.J. Hinde, J.O. Newton, J.R. Leigh, and R.J. Charity, Nucl. Phys. **A398** (1983) 308.

[23] S.Cohen, F. Plasil, and W.J. Swiatecki, Ann. Phys. **82** (1974) 557.

[24] A.J. Sierk, Phys. Rev. **C33** (1986) 2039.

[25] A.J. Sierk, Phys. Rev. Letts. **55** (1985) 582.

[26] L.G. Sobotka, D.G. Sarantites, Z. Li, E.L. Dines, M.L. Halbert, D.C. Hensley, R.P. Schmitt, Z. Majka, G. Nebbia, H.C. Griffin, and A.J. Sierk, Nucl. Phys. **A471** (1987) 131c.

[27] L.G. Sobotka, M.A. McMahan, R.J. McDonald, C. Signarbieux, G.J. Wozniak, M.L. Padgett, J.H. Gu, Z.H. Liu, Z.Q. Yao, and L.G. Moretto, Phys. Rev. Letts. **53** (1984) 2004.

[28] M.C. Mermaz, T. Suomijärvi, R. Lucas, B. Berthier, J. Matuszek, J.P. Coffin, G. Guillaume, B. Heusch, F. Jundt, and F. Rami, Nucl. Phys. **A456** (1986) 186.

[29] J. Galin, L.G. Moretto, R. Babinet, R. Schmitt, R. Jared, and S.G. Thompson, Nucl. Phys. **A258** (1976) 172.

[30] L.G. Moretto, S.K. Kataria, R.C. Jared, R. Schmitt, and S.G. Thompson, Nucl. Phys. **A255** (1975) 491.

[31] R. Babinet, L.G. Moretto, J. Galin, R. Jared, J. Moulton, and S.G. Thompson, Nucl. Phys. **A255** (1975) 472.

[32] C.B. Chitwood, D.J. Fields, C.K. Gelbke, W.G. Lynch, A.D. Panagiotou, M.B. Tsang, H. Utsunomiya, and W.A. Friedman, Phys. Letts. **B131** (1983) 289.

[33] H. Hauser and H. Feshbach, Phys. Rev. **87** (1952) 366.

[34] N. Carjan and J.M. Alexander, Phys. Rev. **C38** (1988) 1692.

[35] R.J. Charity, J.R. Leigh, J.J.M. Bokhorst, A. Chatterjee, G.S. Foote, D.J. Hinde, J.O. Newton, S. Ogaza, and D. Ward, Nucl. Phys. **A457** (1986) 441.

[36] J. van der Plicht, H.C. Britt, M.M. Fowler, Z. Fraenkel, A. Gavron, J.B. Wilhelmy, F. Plasil, T.C. Awes, and G.R. Young, Phys. Rev. **C28** (1983) 2022.

[37] R. Bass, Phys. Rev. Letts. **39** (1977) 265.

[38] W.J. Swiatecki, Nucl. Phys. **A376** (1982) 275.

[39] S. Bjørnholm and W.J. Swiatecki, Nucl. Phys. **A391** (1982) 471.

[40] D.J. Morrissey and L.G. Moretto, Phys. Rev. **C23** (1981) 1835.

[41] L.G. Moretto and R.P. Schmitt, Phys. Rev. **C21** (1979) 204.

[42] R.P. Schmitt and A.J. Pacheco, Nucl. Phys. **A379** (1982) 313.

[43] W. Stocker and J. Burzlaff, Nucl. Phys. **A202** (1973) 265.

[44] G. Suaer, H. Chandra, and U. Mosel, Nucl. Phys. **A264** (1976) 221.

[45] D.G. Ravenhall, C.J. Pethick, and J.M. Lattimer, Nucl. Phys. **A407** (1983) 571.

[46] M. Brack, C. Guet, and H.B. Håkansson, Phys. Rep. **123** (1985) 275.

[47] S. Levit and P. Bonche, Nucl. Phys. **A437** (1985) 426.

[48] M.G. Mustafa in *Proceedings of the All-Union Symposium on the Physics of Nuclear Fission, Obninsk, USSR*, June 2-5 1987.

[49] B. Heusch, C. Volant, H. Freiesleben, R.P. Chestnut, K.D. Hildenbrand, F. Pühlhofer, W.F.W. Schneider, B. Kohlmeyer, and W. Pfeffer, Z. Phys. **A288** (1978) 391.

[50] C. Lebrun, F. Hanappe, J.F. Lecolley, F. Lefebvres, C. Ngô, J. Péter, and B. Tamain, Nucl. Phys. **A321** (1979) 207.

[51] B. Borderie, M. Berlanger, D. Gardès, F. Hanappe, L. Nowicki, J. Péter, B. Tamain, S. Agarwal, J. Girard, C. Grégoire, J. Matuszek, and C. Ngô, Z. Phys. **A299** (1981) 263.

[52] B. Heusch, H. Freiesleben, W.F.W Schneider, B. Kohlmeyer, H. Stege, and F. Pühlhofer, Z. Phys. **A322** (1985) 309.

[53] C. Grégoire, C. Ngô, and B. Remaud, Nucl. Phys. **A383** (1982) 392.

[54] D. Hilscher, H. Rossner, B. Cramer, B. Gebauer, U. Jahnke, E. Schwinn, M. Wilpert, Th. Wilpert, H. Frobeen, E. Mordhorst, and W. Scobel, Phys. Rev. Letts. **62** (1989) 1099.

[55] R.J. Charity. private communication.

[56] B.V. Jacak, G.D. Westfall, C.K. Gelbke, L.H. Harwood, W.G. Lynch, D.K. Scott, H. Stöker, M.B. Tsang, and T.J.M. Symons, Phys. Rev. Letts. **51** (1983) 1846.

[57] D.J. Fields, W.G. Lynch, C.B. Chitwood, C.K. Gelbke, M.B. Tsang, H. Utsunomiya, and J. Aichelin, Phys. Rev. **C30** (1984) 1912.

[58] H. Machner, Phys. Rev. **C31** (1985) 1271.

# Figures

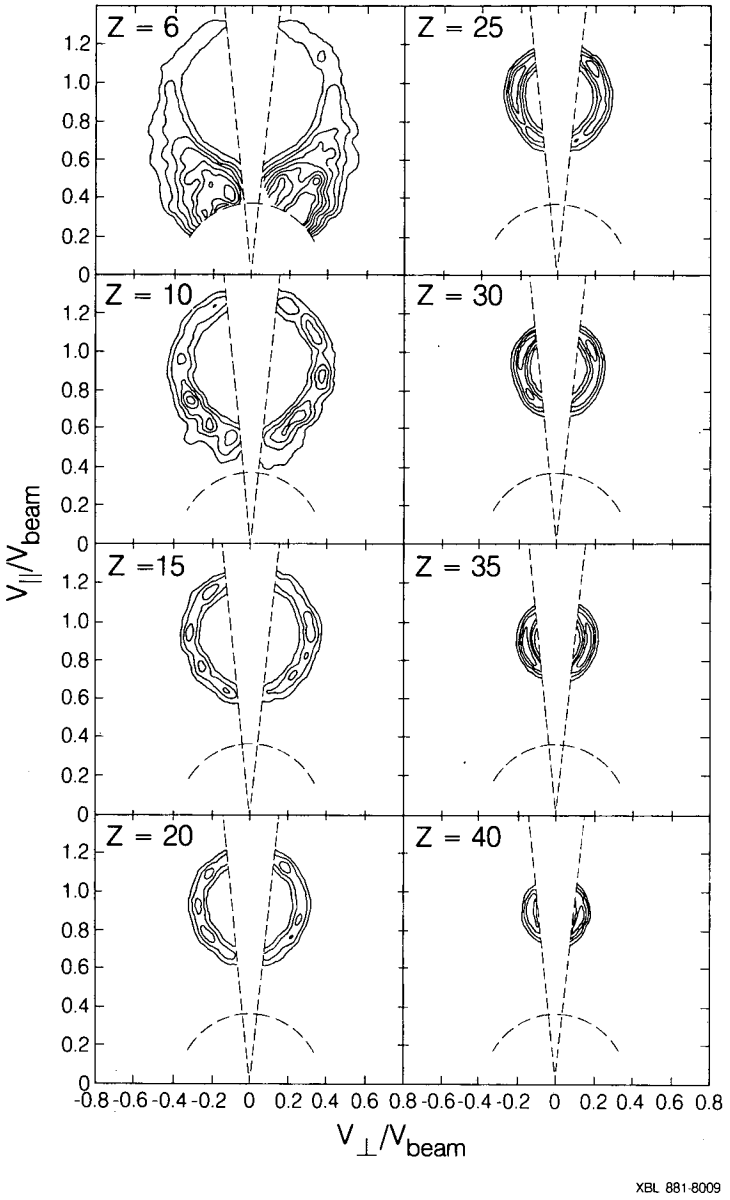
E/A = 18 MeV $^{139}$La + $^{12}$C
Z = 6
Z = 25
Z = 10
Z = 30
Z =15
Z = 35
Z = 20
Z = 40
$V_{||}/V_{beam}$
$V_{\perp}/V_{beam}$
XBL 881-8009

Fig. 1

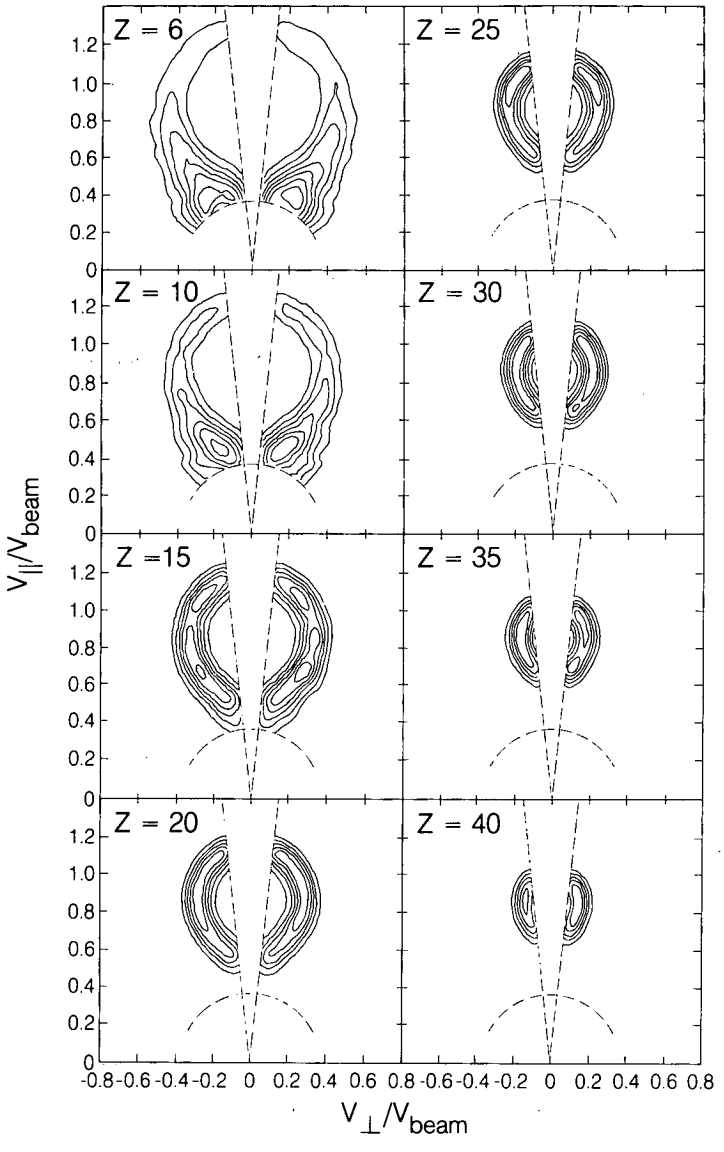
E/A = 18 MeV $^{139}$La + $^{27}$Al
Z = 6
Z = 25
Z = 10
Z = 30
Z =15
Z = 35
Z = 20
Z = 40
$V_{||}/V_{beam}$
$V_{\perp}/V_{beam}$
XBL 881-8010

Fig. 2

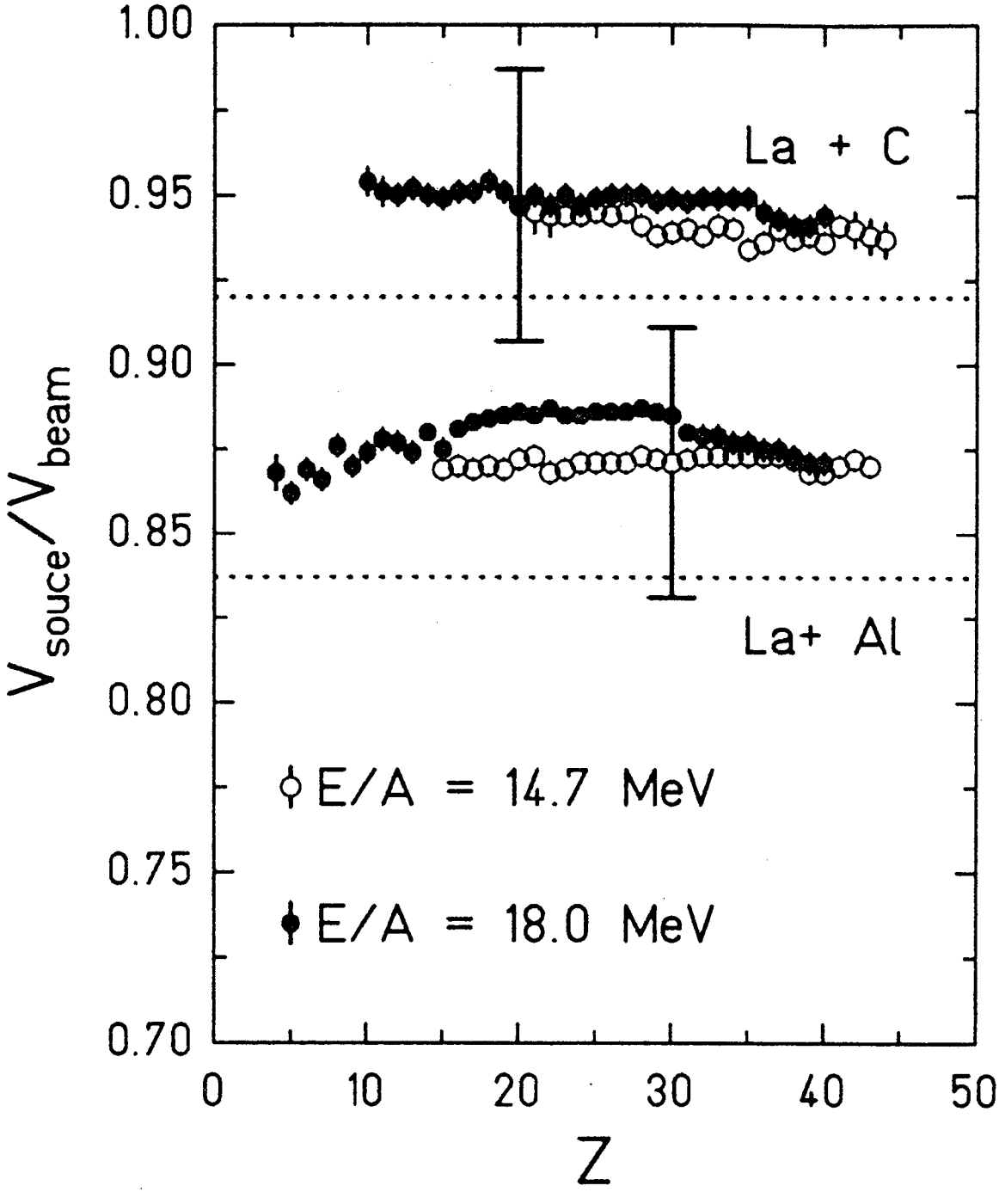


XBL 895-1945

Fig. 3

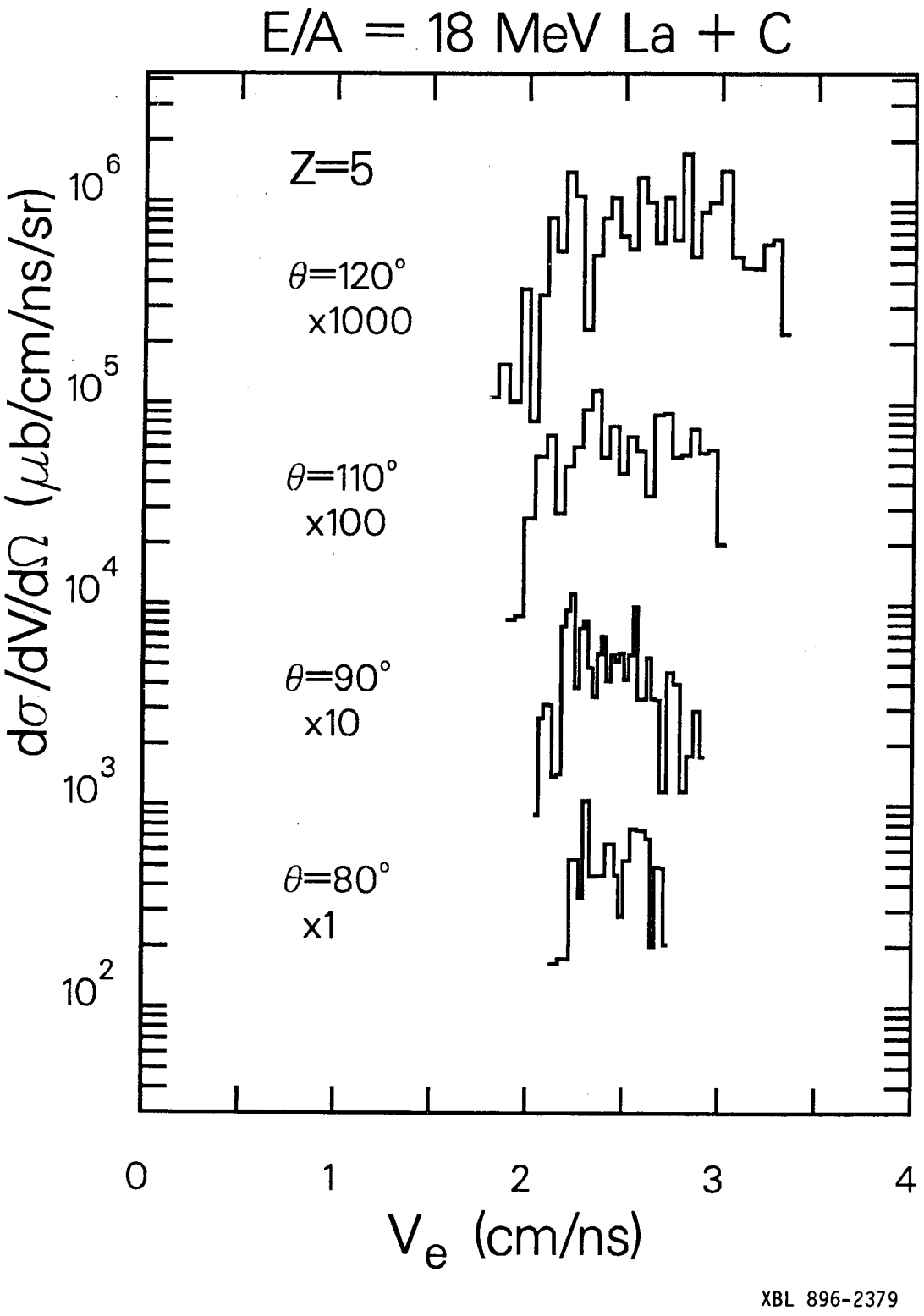
E/A = 18 MeV La + C
Z=5
θ=120°
x1000
θ=110°
x100
θ=90°
x10
θ=80°
x1
dσ/dV/dΩ (μb/cm/ns/sr)
10^6
10^5
10^4
10^3
10^2
0
1
2
3
4
V_e (cm/ns)
XBL 896-2379

Fig. 4

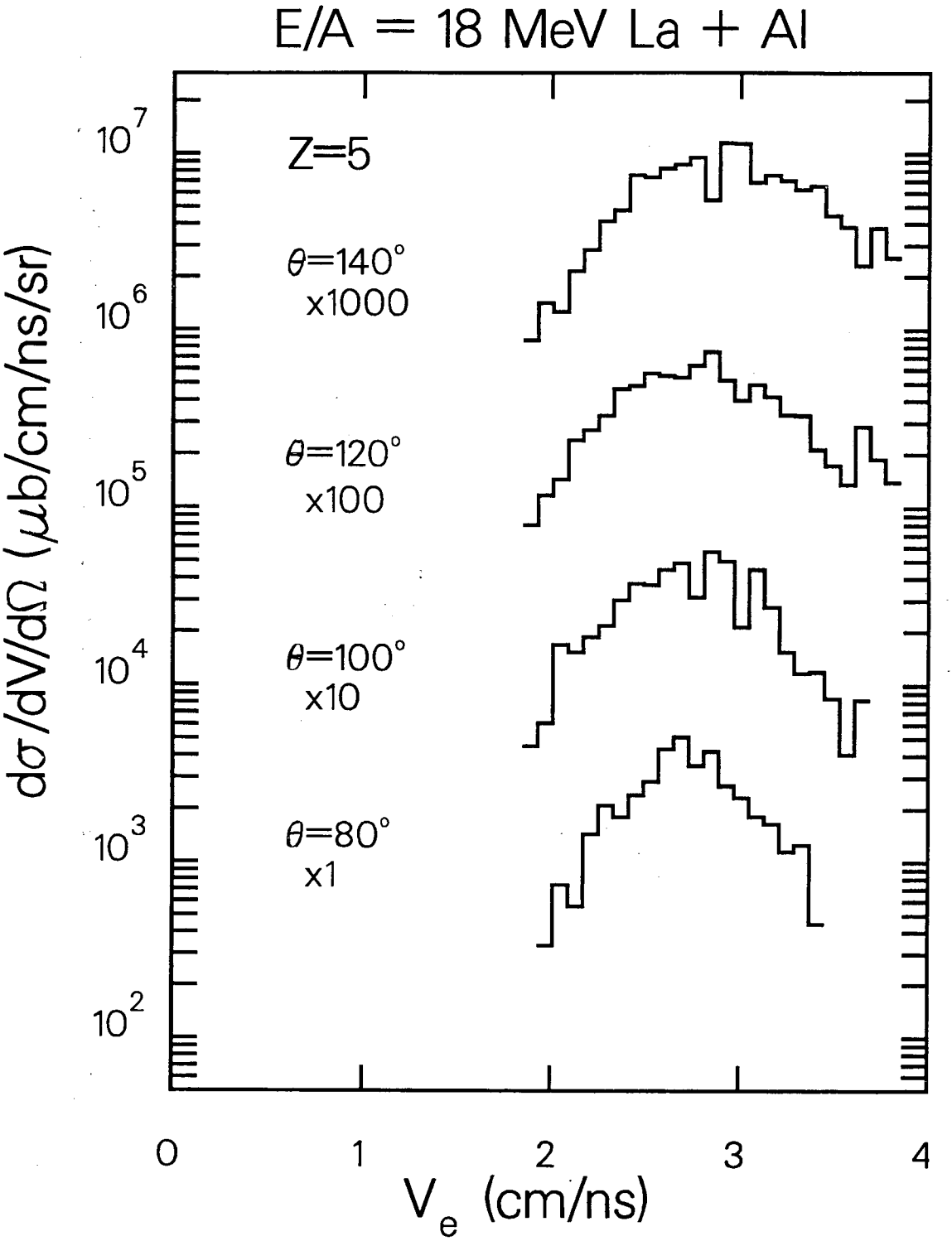


XBL 896-2380

Fig. 5

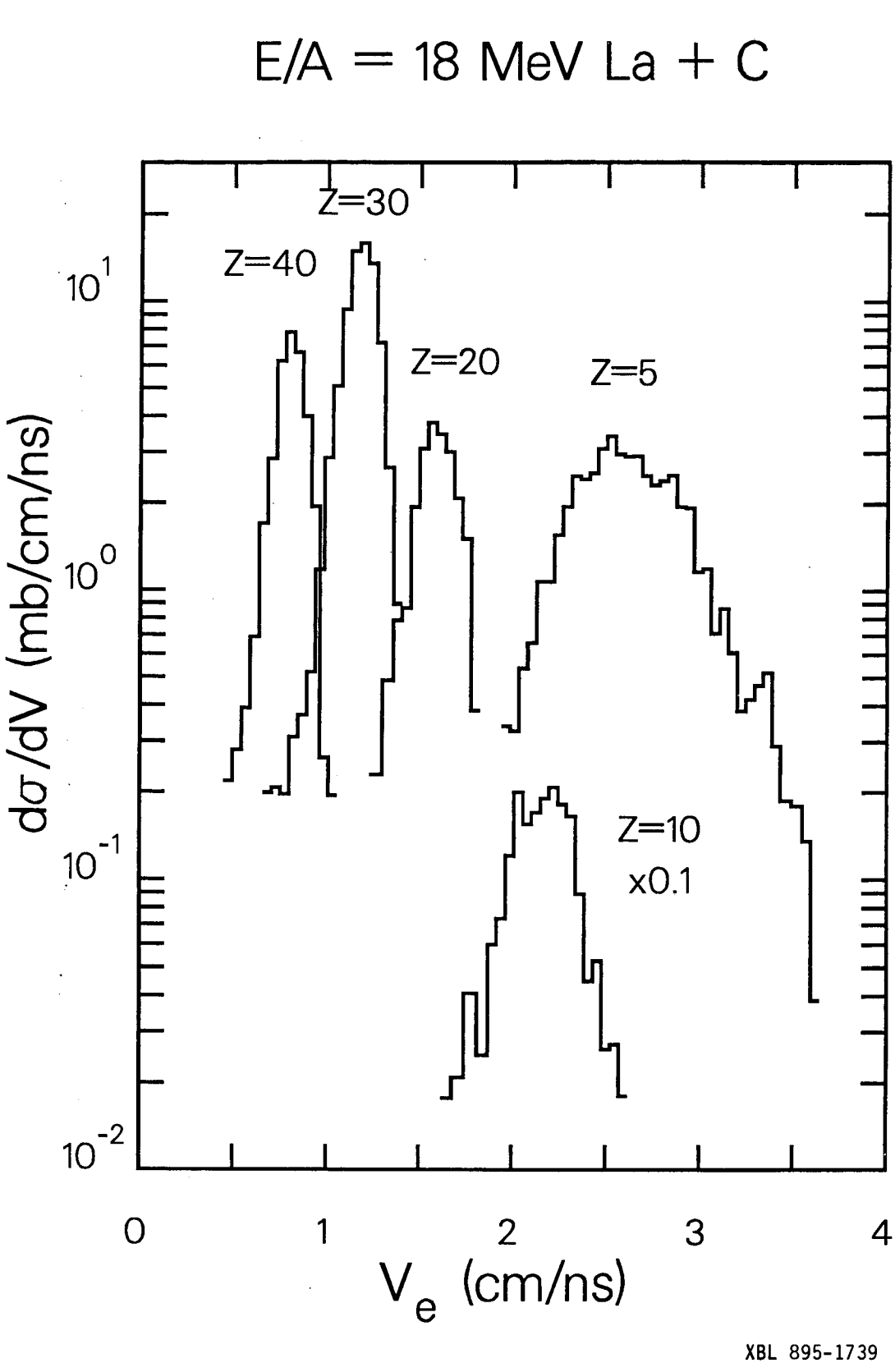
E/A = 18 MeV La + C
Z=30
Z=40
Z=20
Z=5
Z=10
x0.1
$10^{1}$
$10^{0}$
$10^{-1}$
$10^{-2}$
dσ/dV (mb/cm/ns)
0
1
2
3
4
$V_e$ (cm/ns)
XBL 895-1739

Fig. 6

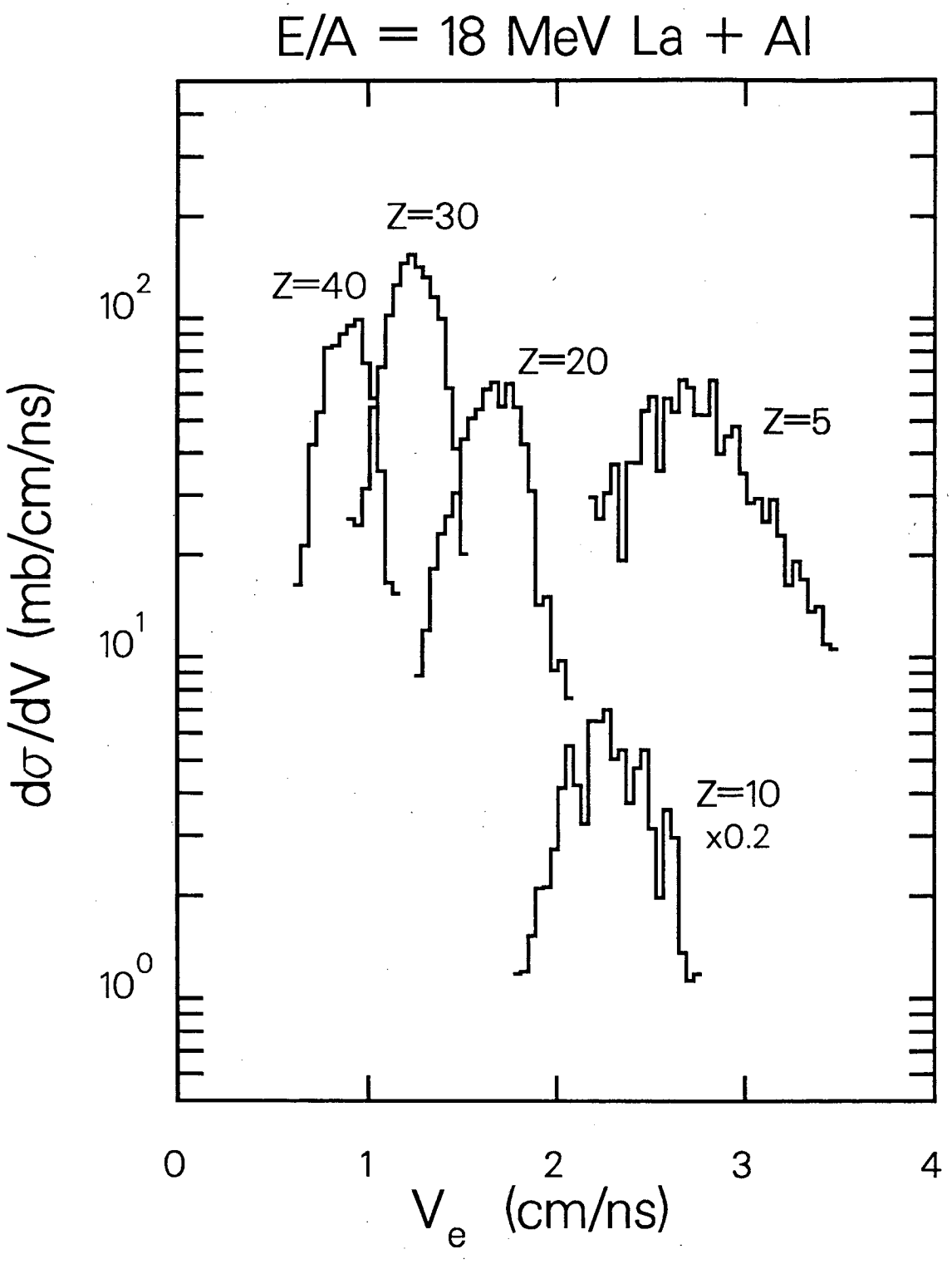
E/A = 18 MeV La + Al
Z=30
Z=40
Z=20
Z=5
Z=10
x0.2
$10^2$
$10^1$
$10^0$
dσ/dV (mb/cm/ns)
0
1
2
3
4
$V_e$ (cm/ns)
XBL 895-1742

Fig. 7

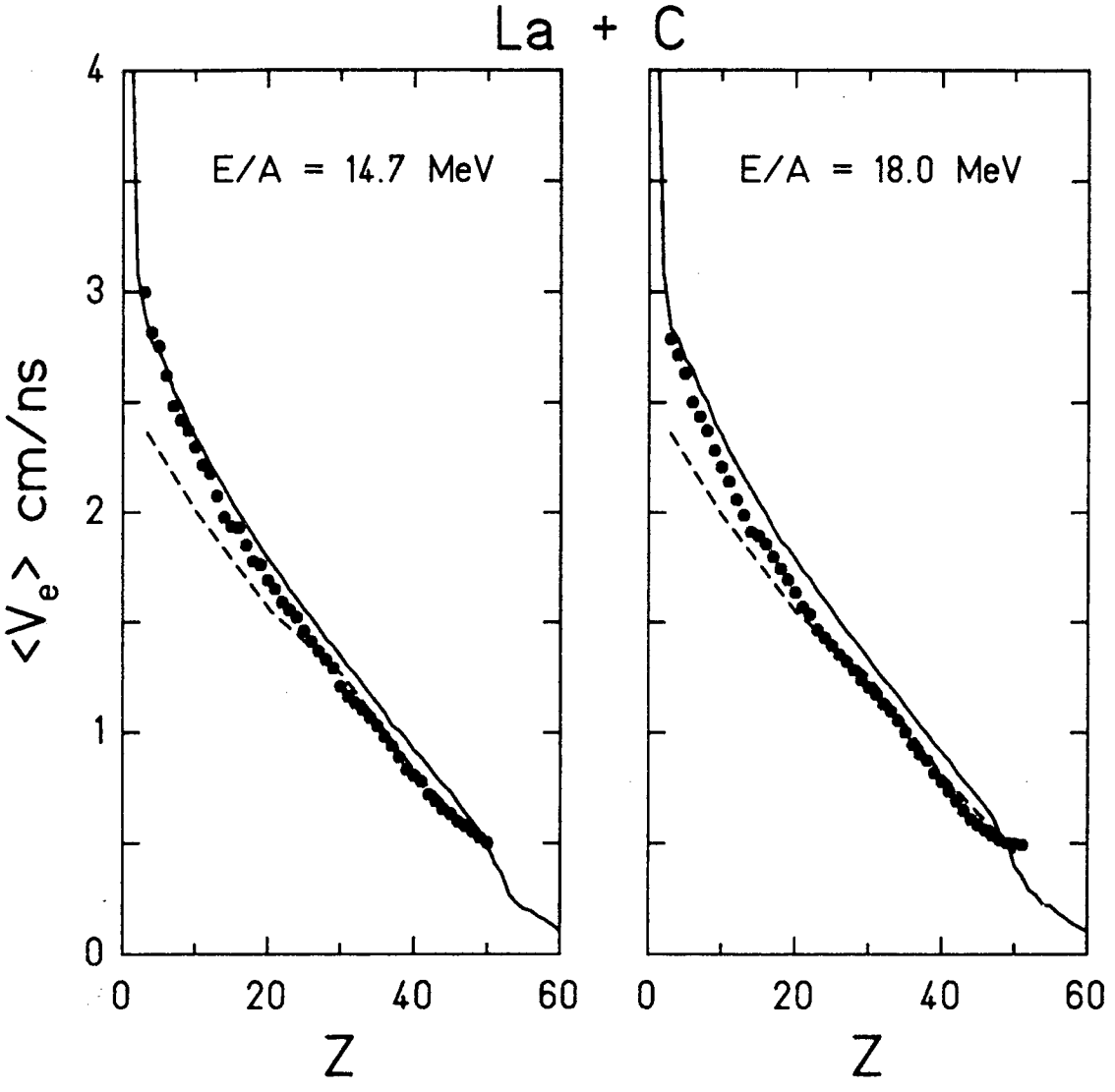


XBL 895-1946

Fig. 8

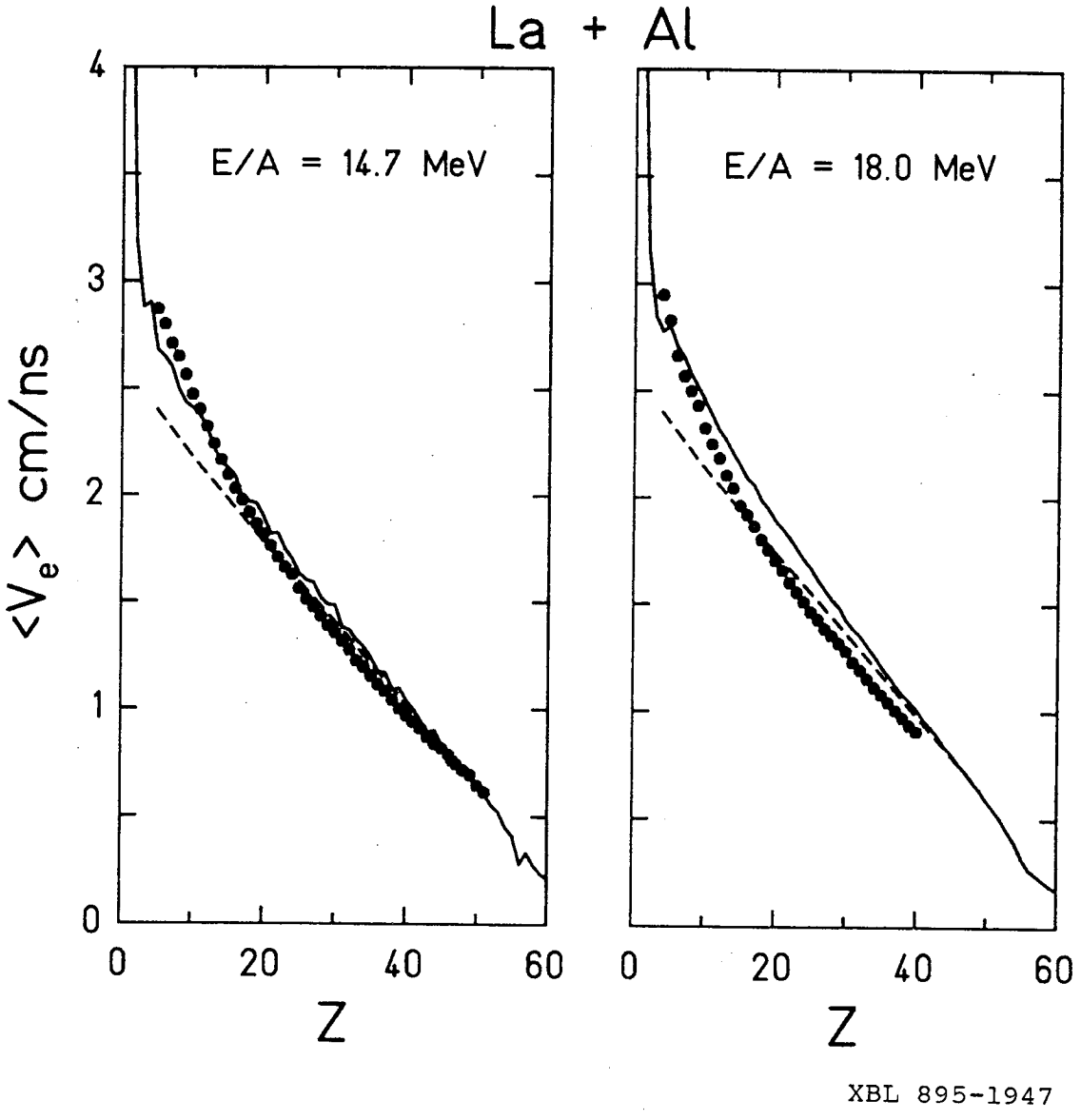
La + Al
E/A = 14.7 MeV
E/A = 18.0 MeV
<Ve> cm/ns
Z
Z
0
1
2
3
4
0
20
40
60
0
20
40
60
XBL 895-1947

Fig. 9

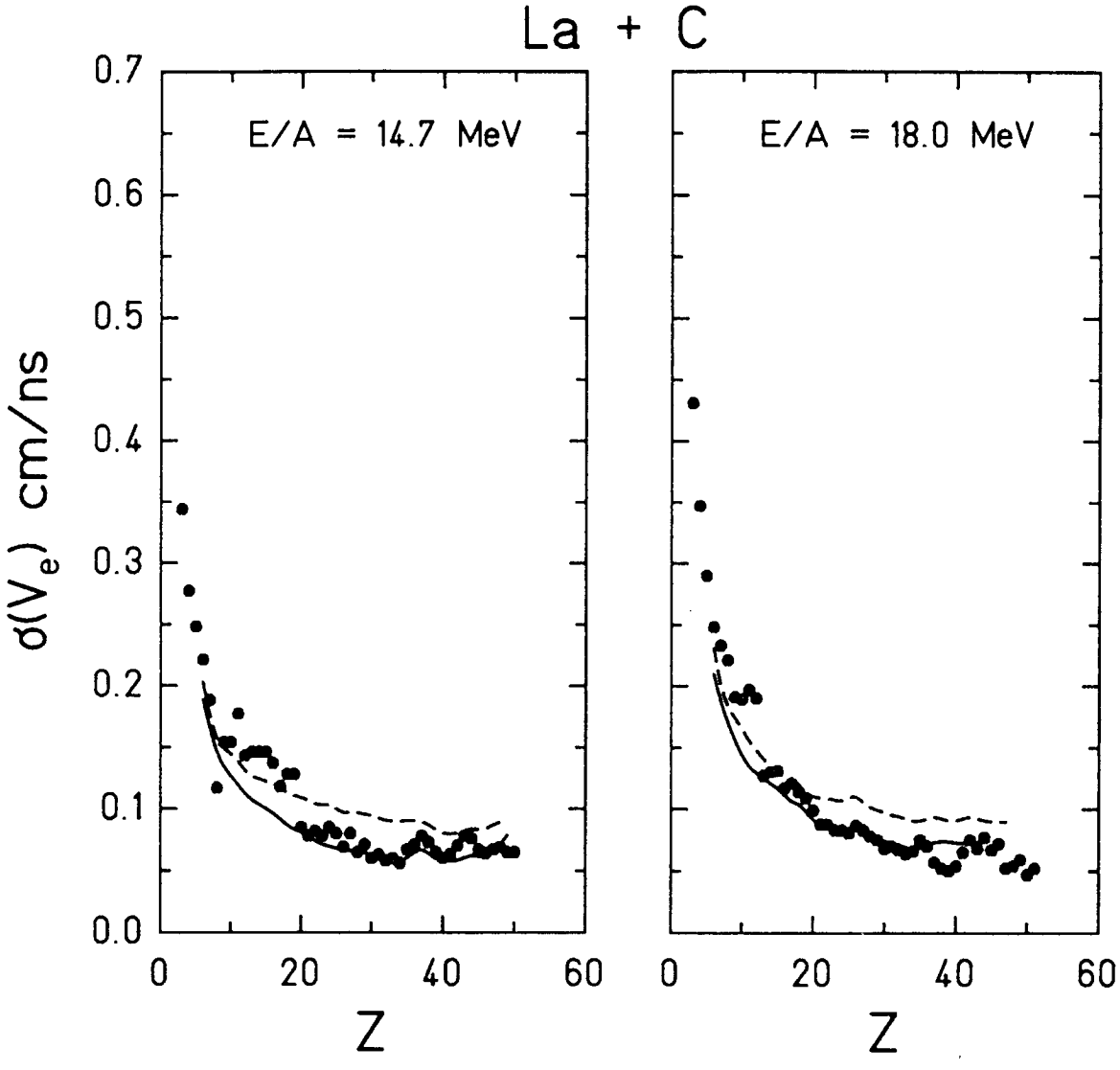
La + C
E/A = 14.7 MeV
E/A = 18.0 MeV
σ(V_e) cm/ns
0.0
0.1
0.2
0.3
0.4
0.5
0.6
0.7
0
20
40
60
Z
Z
XBL 895-1948

Fig. 10

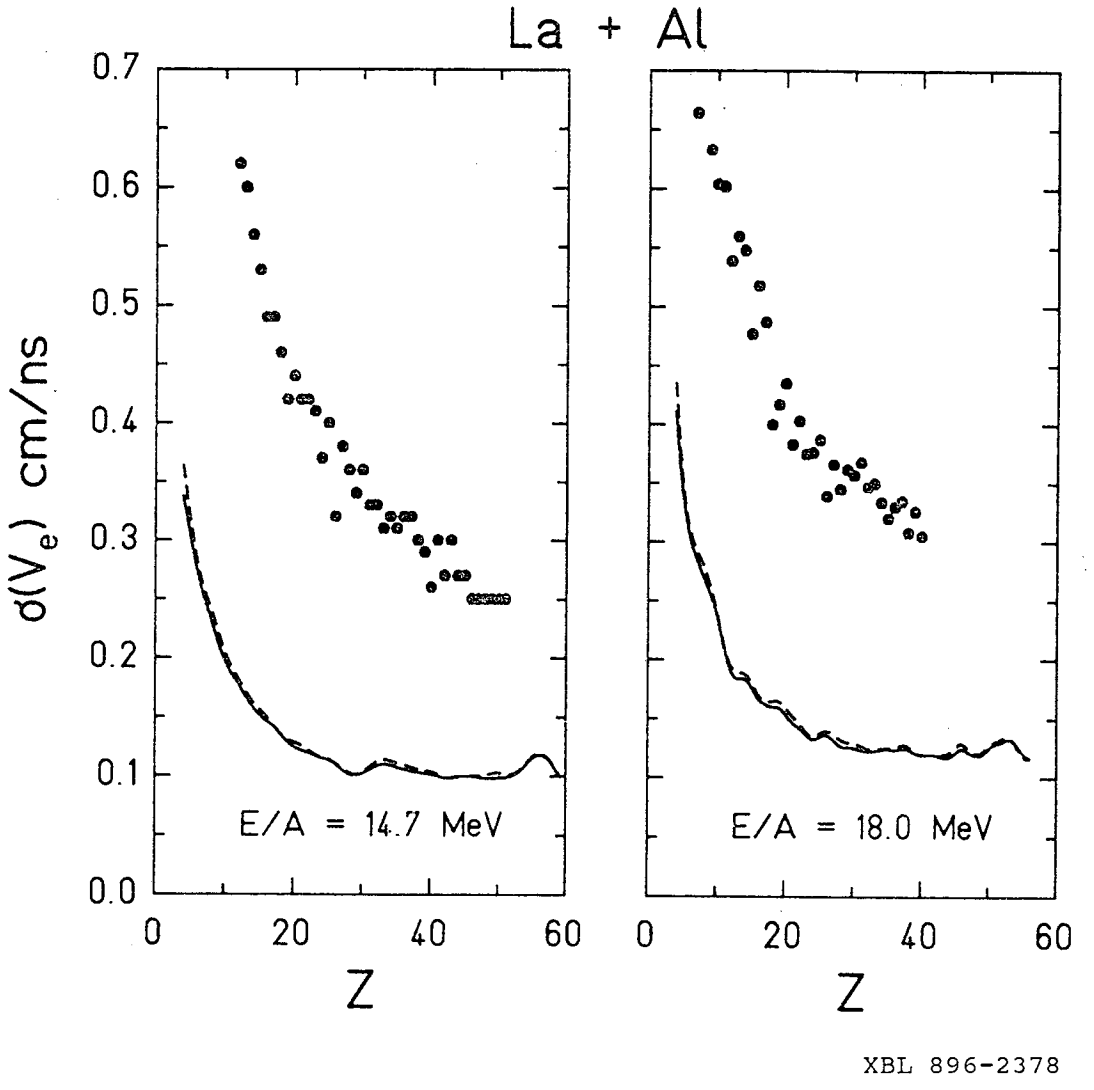
La + Al
0.7
0.6
0.5
0.4
0.3
0.2
0.1
0.0
σ(V_e) cm/ns
E/A = 14.7 MeV
E/A = 18.0 MeV
0
20
40
60
Z
XBL 896-2378

Fig. 11

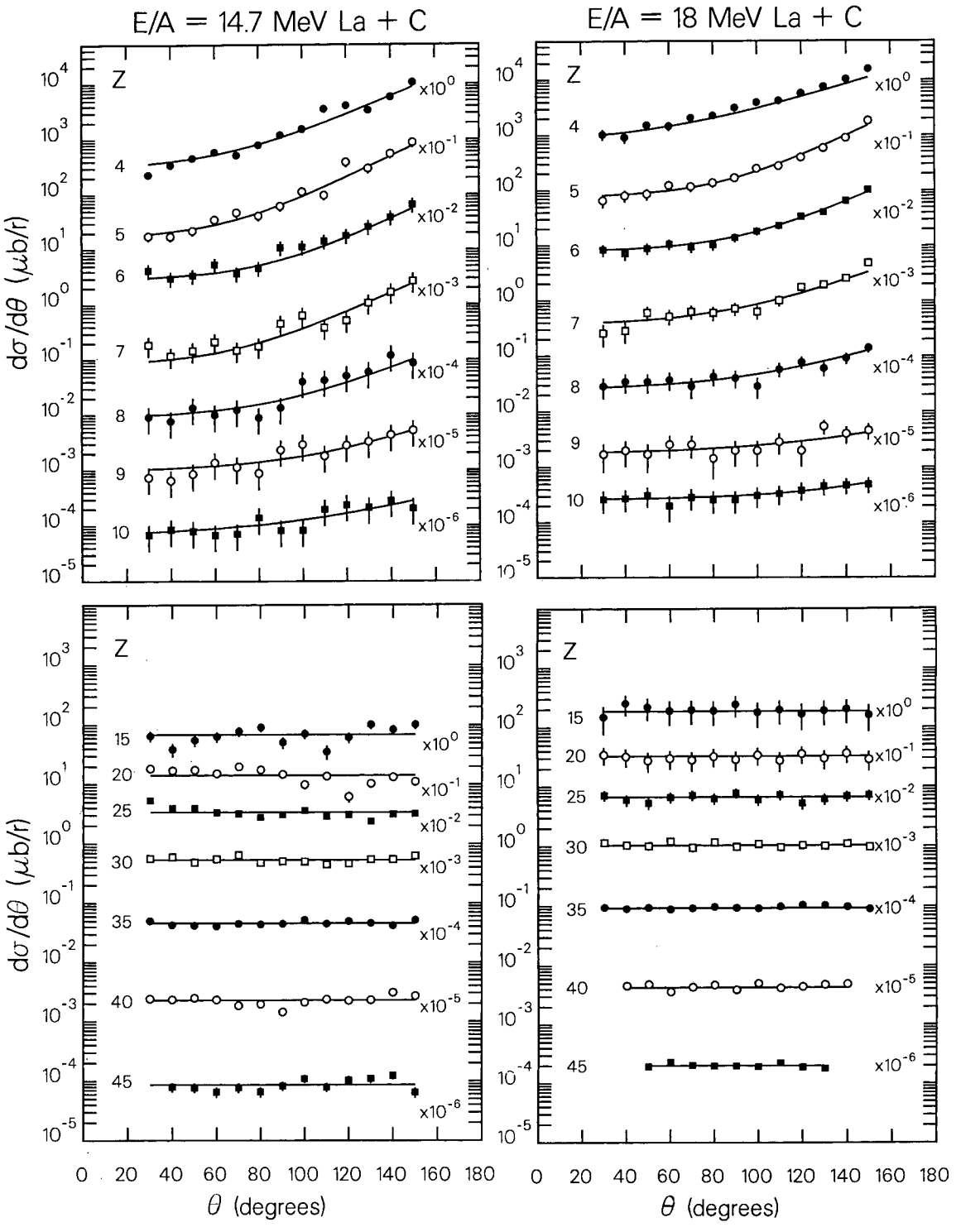


XBL 895-1746 A

Fig. 12

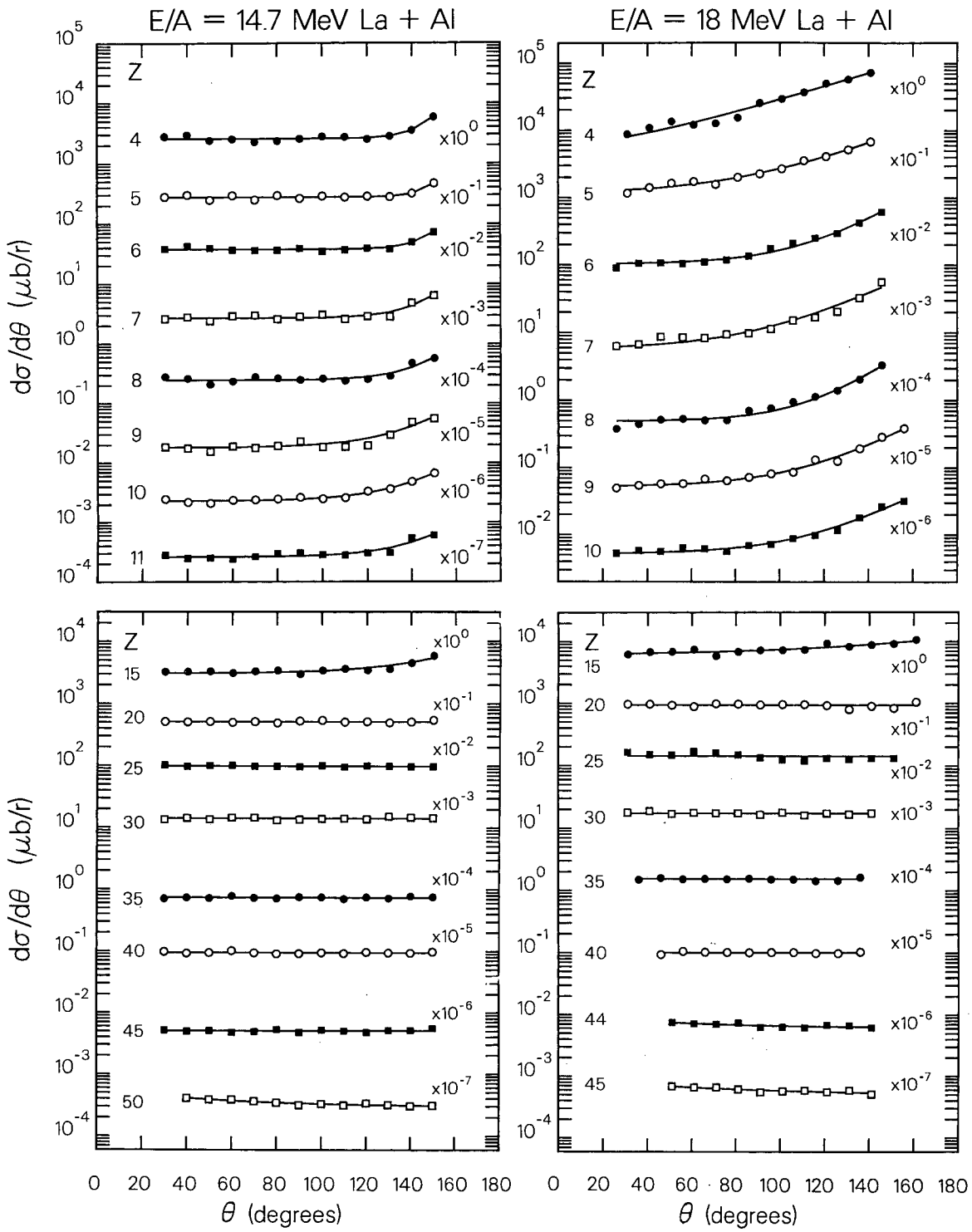


Fig. 13

XBL 895-1747 A

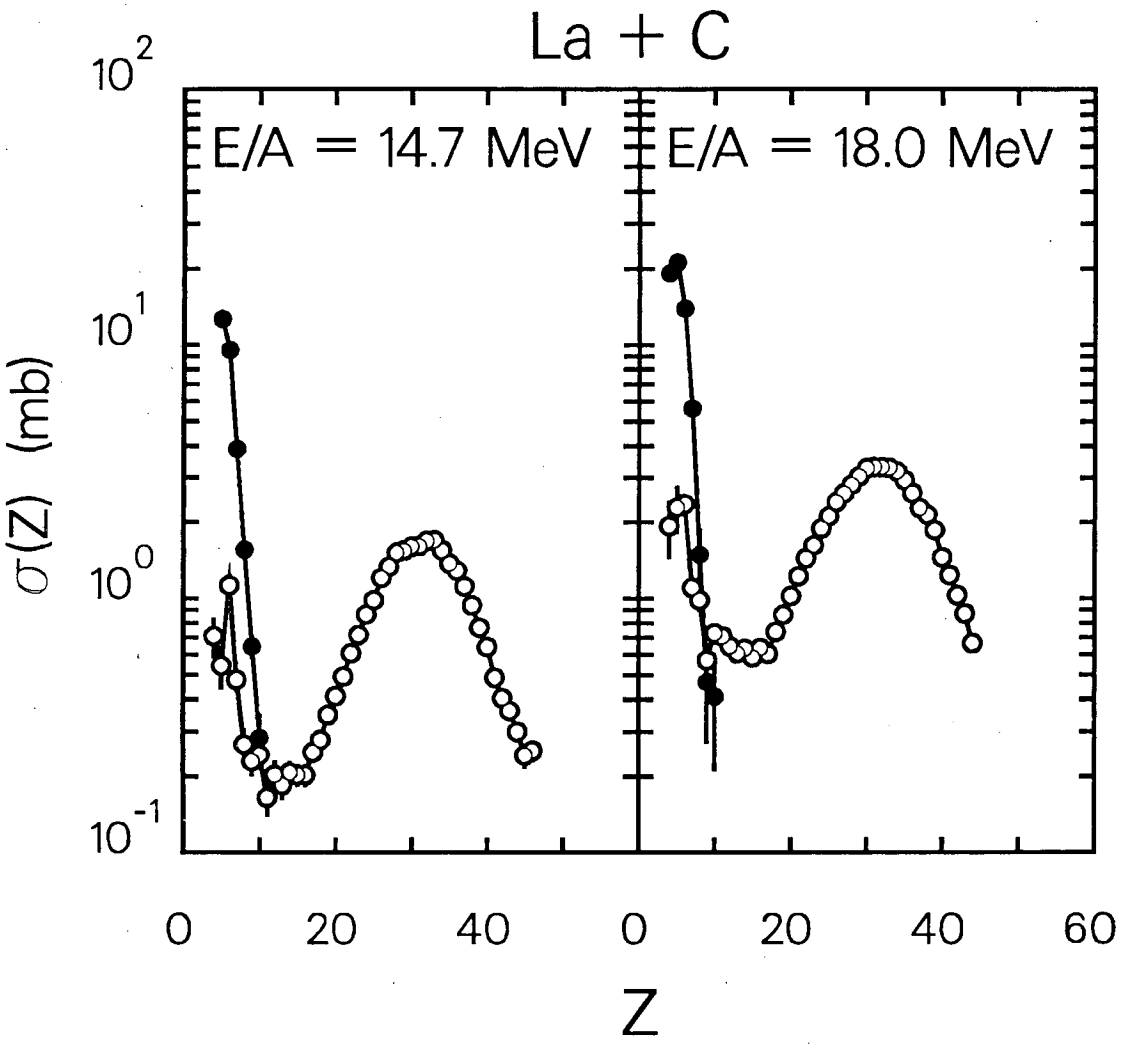


XBL 895-1743

Fig. 14

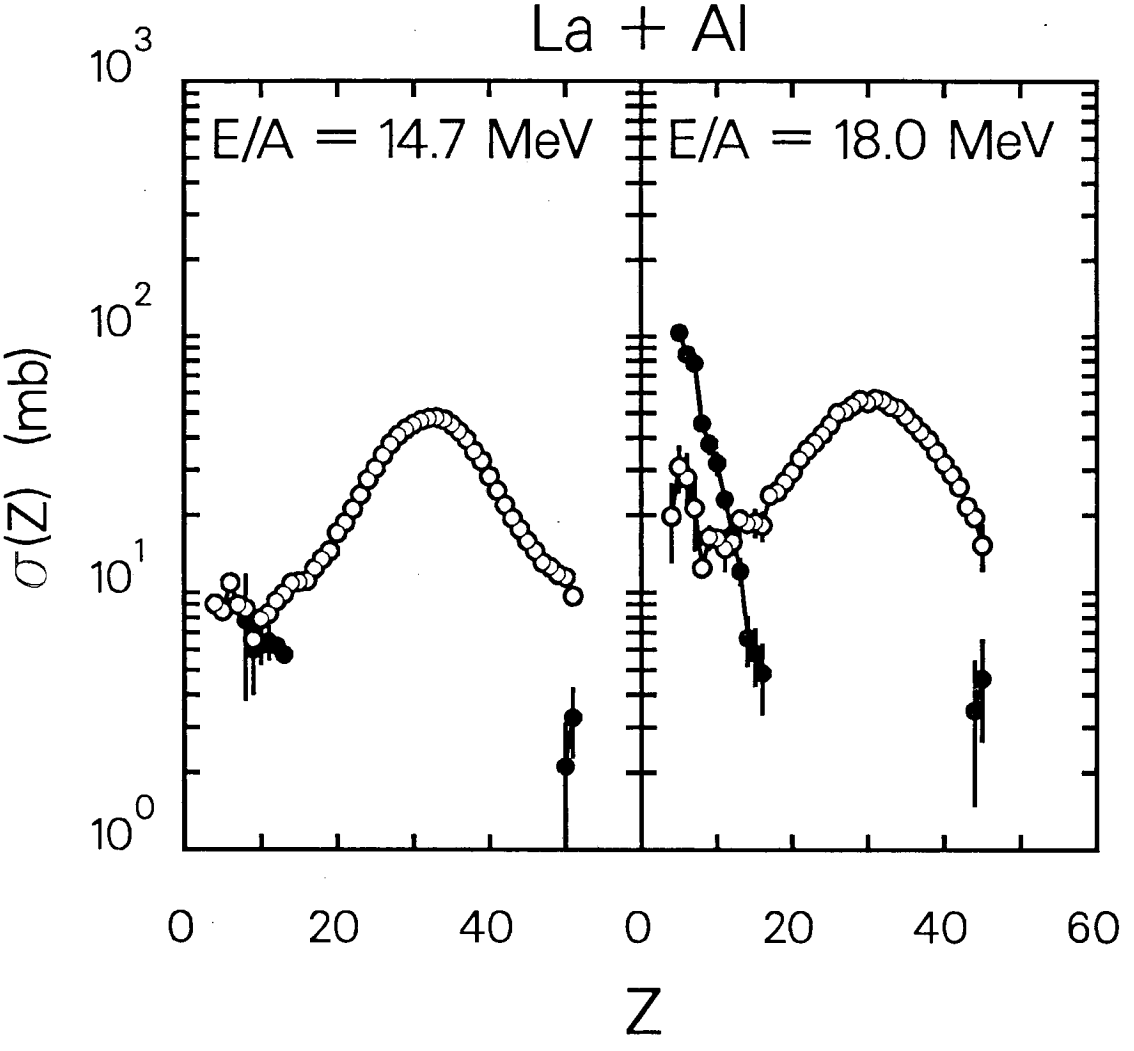
La + Al
E/A = 14.7 MeV
E/A = 18.0 MeV
σ(Z) (mb)
10^3
10^2
10^1
10^0
0
20
40
0
20
40
60
Z
XBL 895-1744

Fig. 15

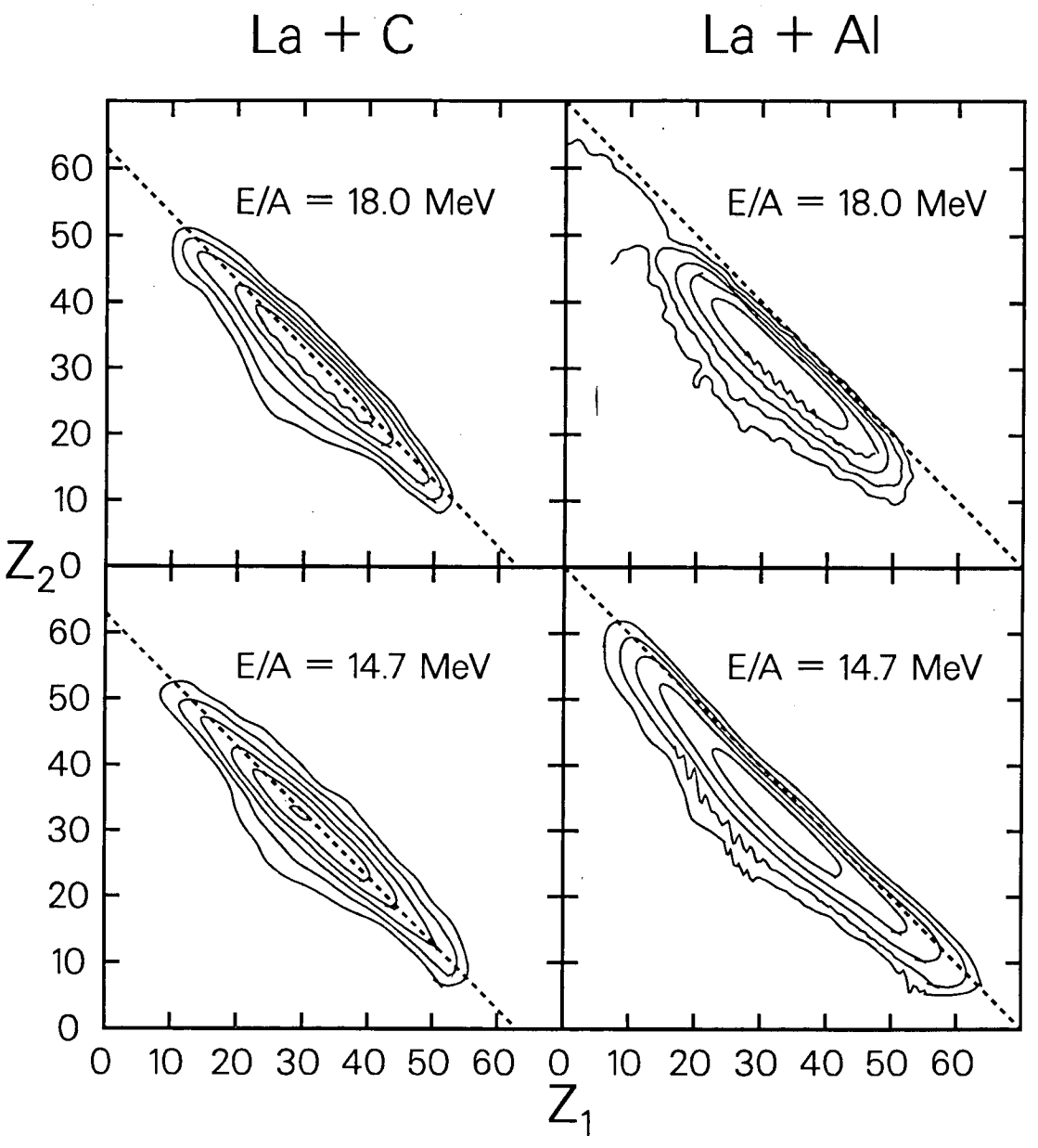


XBL 895-1745

Fig. 16

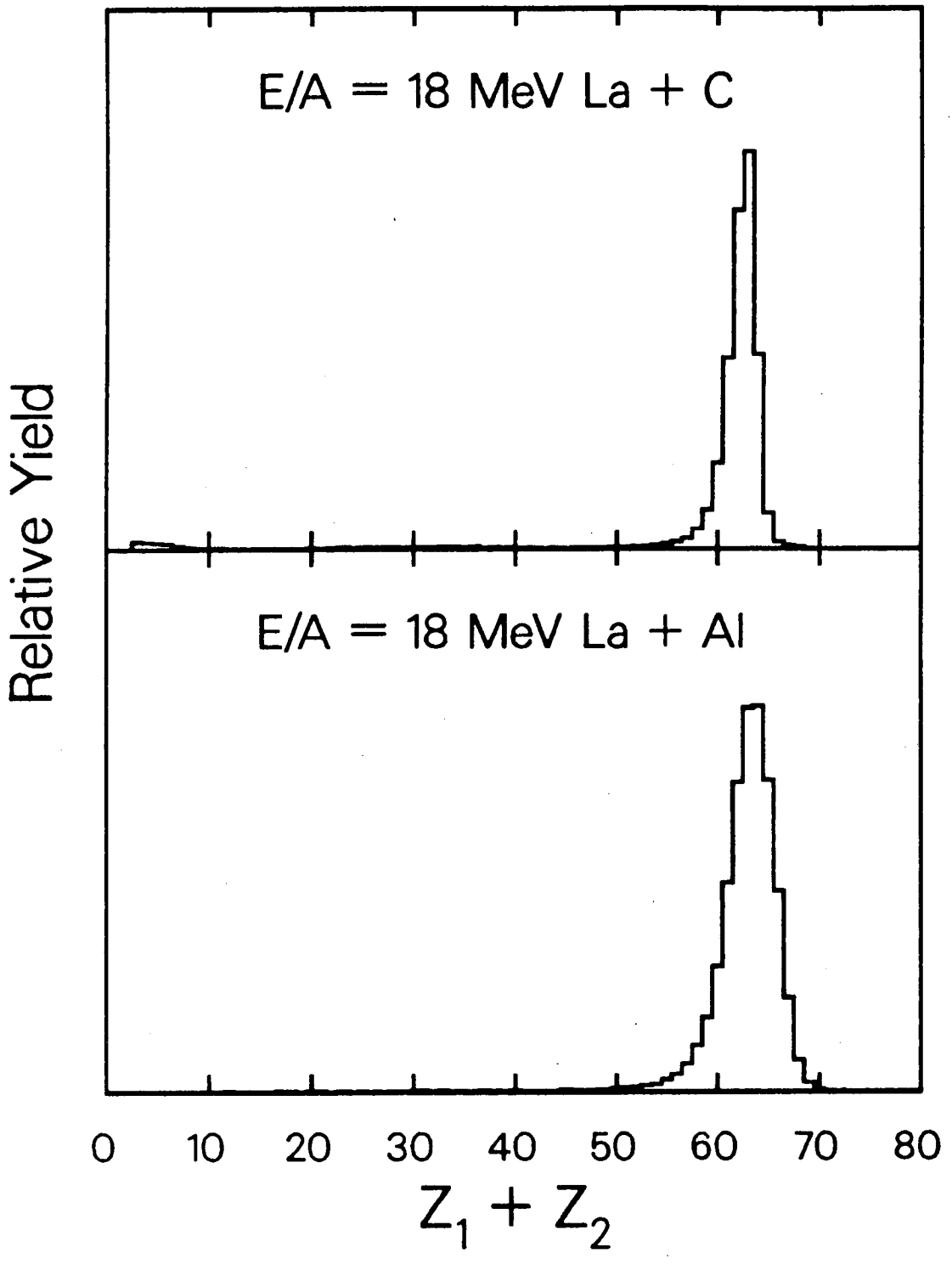


XBL 8712-5372

Fig. 17

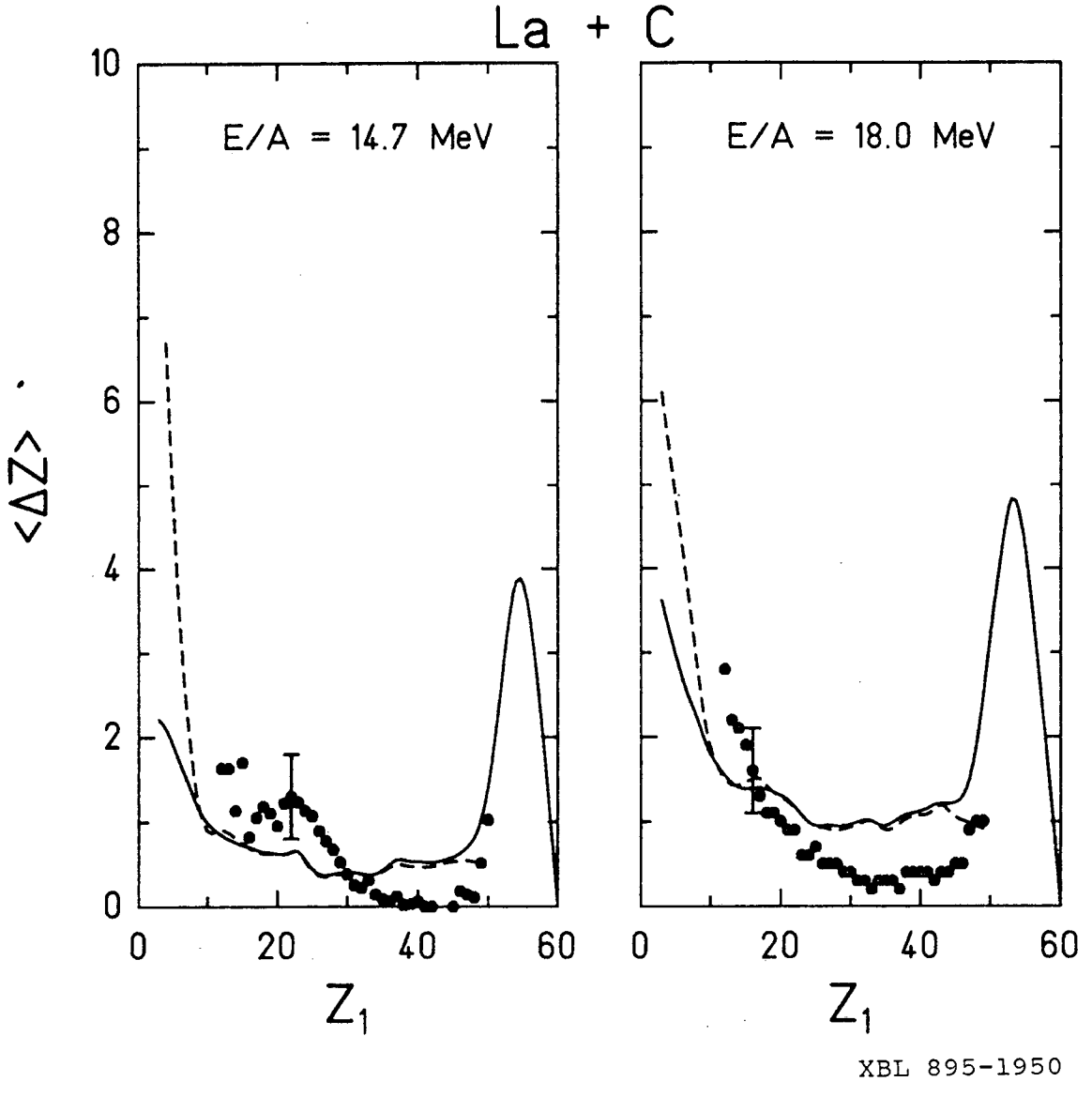


Fig. 18

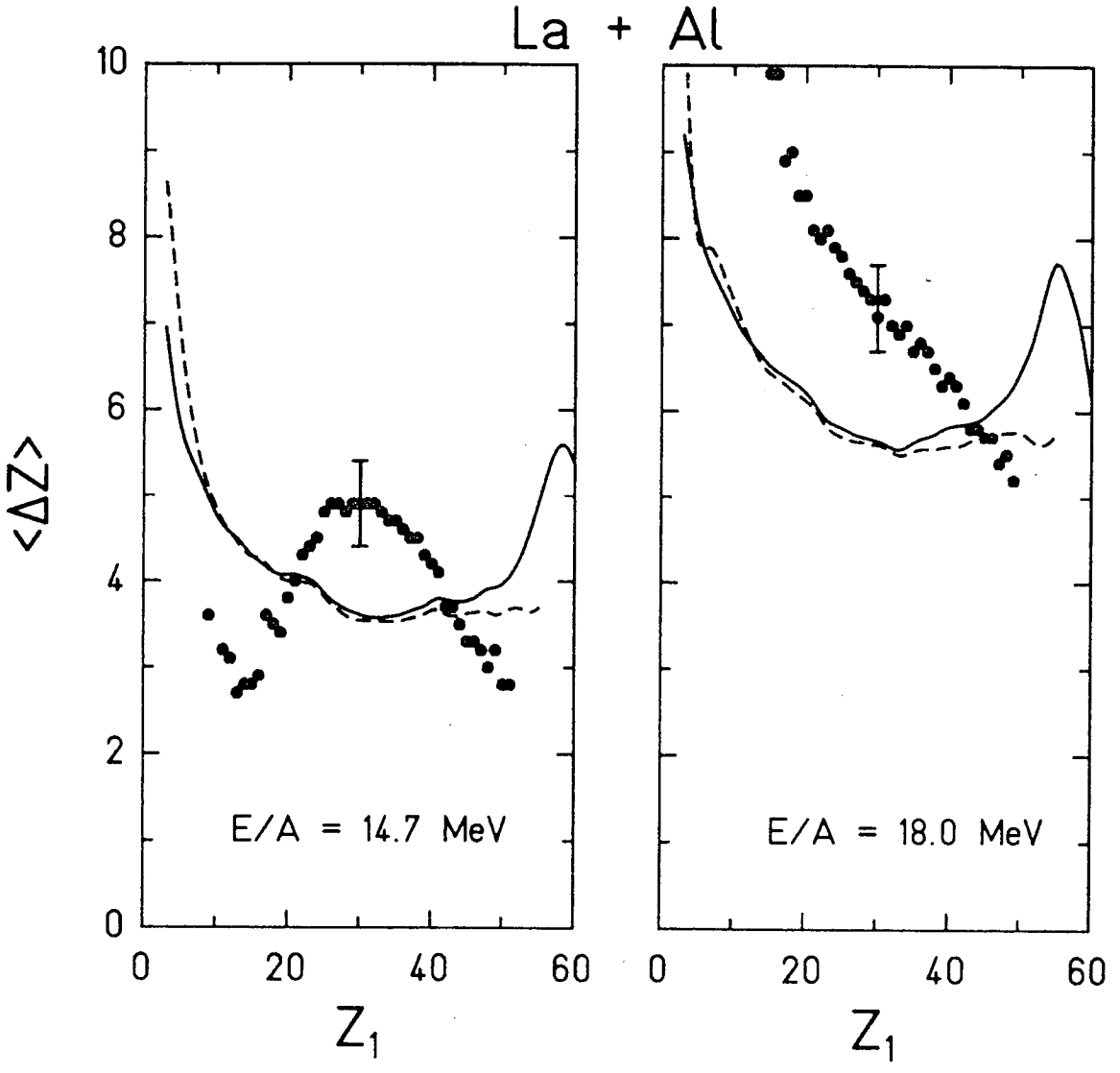


XBL 895-1951

Fig. 19

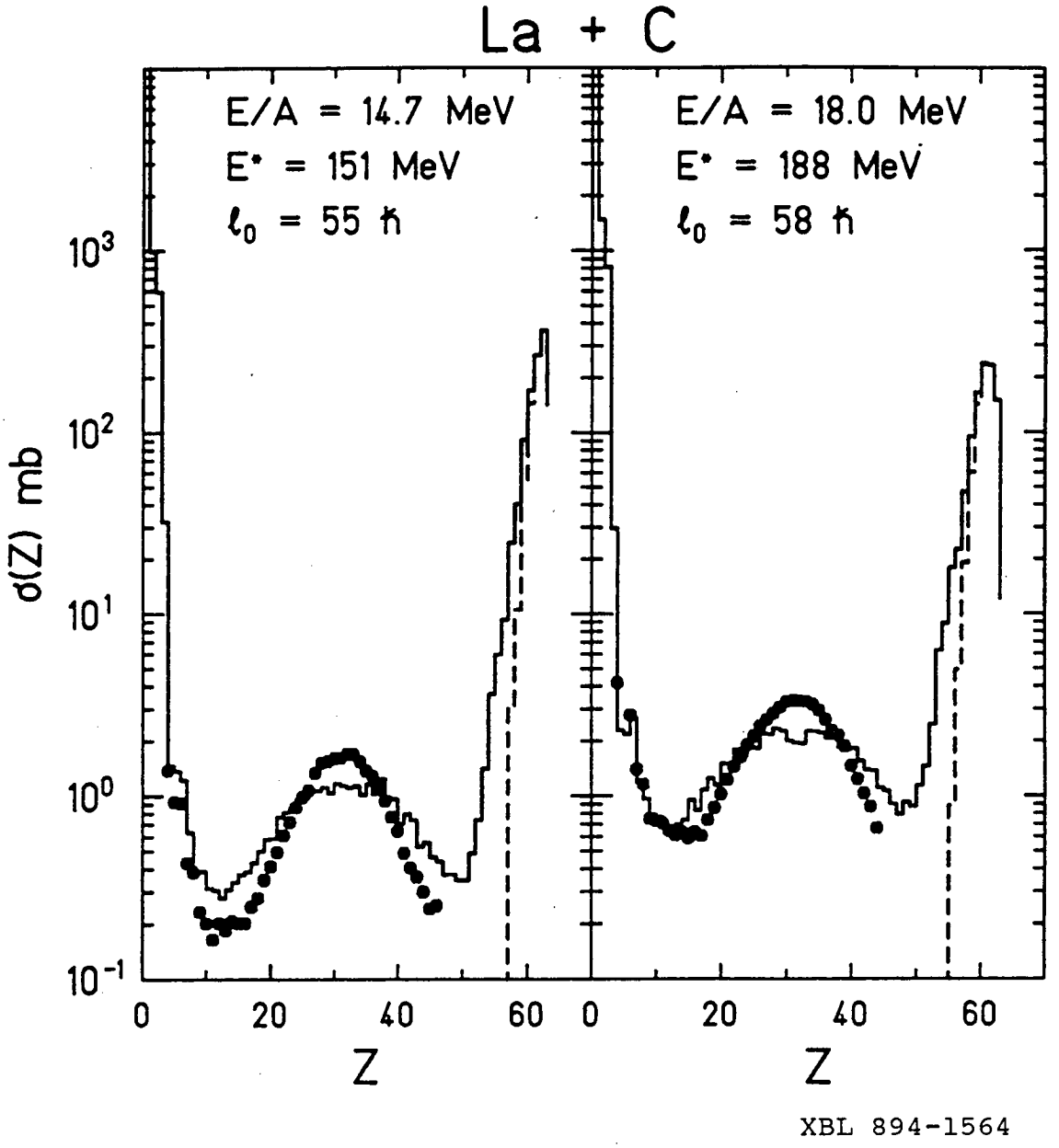
La + C
E/A = 14.7 MeV
E* = 151 MeV
ℓ0 = 55 ħ
E/A = 18.0 MeV
E* = 188 MeV
ℓ0 = 58 ħ
σ(Z) mb
10^3
10^2
10^1
10^0
10^-1
0
20
40
60
Z
XBL 894-1564

Fig. 20

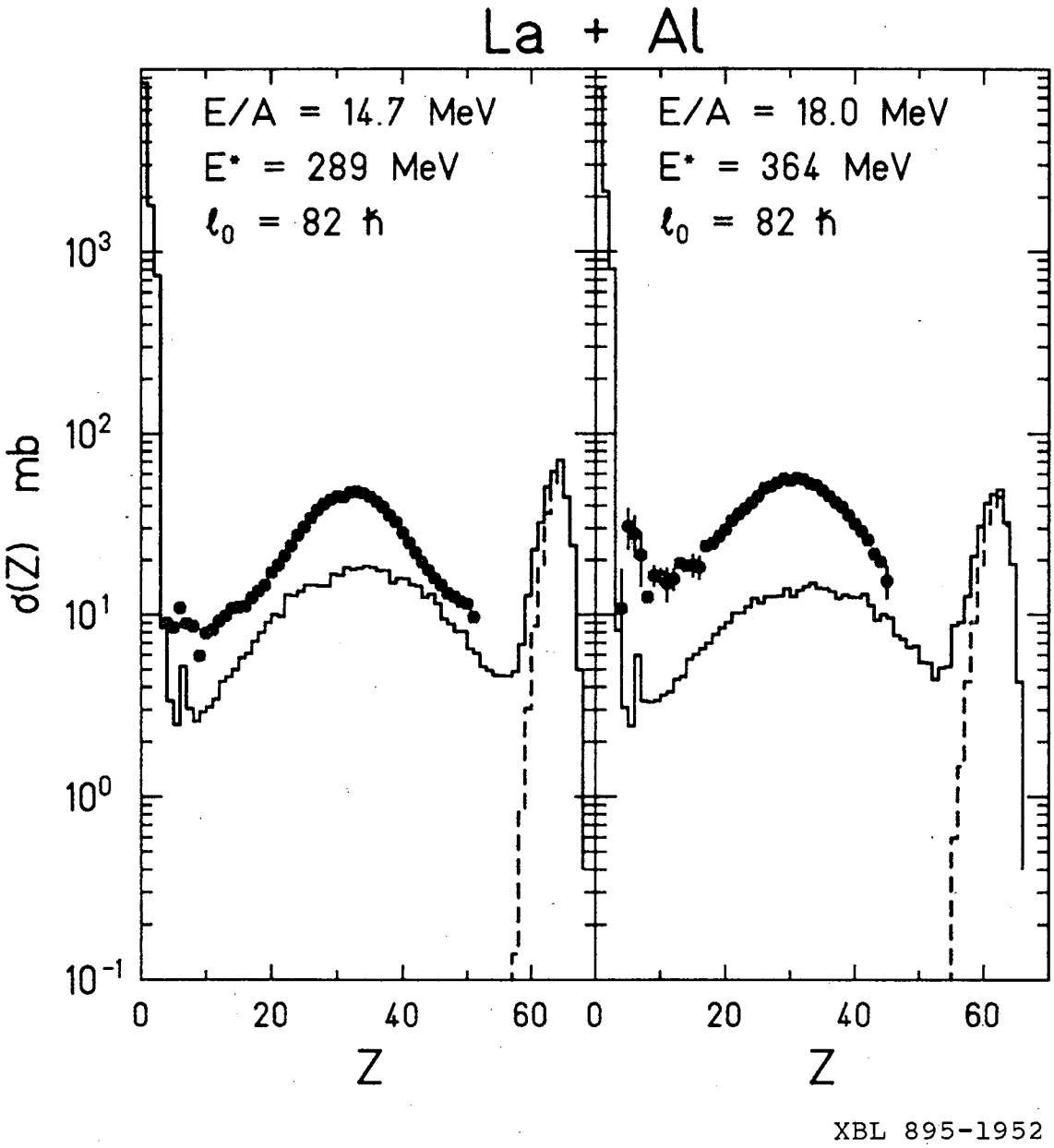
La + Al
E/A = 14.7 MeV
E* = 289 MeV
ℓ0 = 82 ħ
E/A = 18.0 MeV
E* = 364 MeV
ℓ0 = 82 ħ
σ(Z) mb
10^3
10^2
10^1
10^0
10^-1
0
20
40
60
Z
XBL 895-1952

Fig. 21

LAWRENCE BERKELEY LABORATORY
TECHNICAL INFORMATION DEPARTMENT
1 CYCLOTRON ROAD
BERKELEY, CALIFORNIA 94720